Posted on 30 Nov 2022 — The copyright holder is the author/funder. All rights reserved. No reuse without permission. — https://doi.org/10.1002/essoar.10501078/v3 — This a preprint and has not been peer reviewed. Data may be preliminary.

Can the Last Interglacial Constrain Projections of Future Antarctic Ice Mass Loss and Sea-level Rise?

Daniel Gilford[1,1,1], Erica Ashe[1,1,1], Robert Kopp[1,1,1], Robert DeConto[2,2,2], David Pollard[3,3,3], and Alessio Rovere[4,4,4]

[1]Rutgers University
[2]University of Massachusetts Amherst
[3]Pennsylvania State University
[4]Universität Bremen

November 30, 2022

Abstract

Previous studies have interpreted Last Interglacial (LIG; ˜129–116 ka) sea-level estimates in multiple different ways to calibrate projections of future Antarctic ice-sheet (AIS) mass loss and associated sea-level rise. This study systematically explores the extent to which LIG constraints could inform future Antarctic contributions to sea-level rise. We develop a Gaussian process emulator of an ice-sheet model to produce continuous probabilistic projections of Antarctic sea-level contributions over the LIG and a future high-emissions scenario. We use a Bayesian approach conditioning emulator projections on a set of LIG constraints to find associated likelihoods of model parameterizations. LIG estimates inform both the probability of past and future ice-sheet instabilities and projections of future sea-level rise through 2150. Although best-available LIG estimates do not meaningfully constrain Antarctic mass loss projections or physical processes through 2060, they become increasingly informative over the next 130 years. Uncertainties of up to 50 cm remain in future projections even if LIG Antarctic mass loss is precisely known (+/- 5 cm), indicating there is a limit to how informative the LIG could be for ice-sheet model future projections. The efficacy of LIG constraints on Antarctic mass loss also depends on assumptions about the Greenland ice sheet and LIG sea-level chronology. However, improved field measurements and understanding of LIG sea-levels still have potential to improve future sea-level projections, highlighting the importance of continued observational efforts.

Could the Last Interglacial Constrain Projections of Future Antarctic Ice Mass Loss and Sea-level Rise?

Daniel M. Gilford[1,2], Erica L. Ashe[2], Robert M. DeConto[3], Robert E. Kopp[1,2], David Pollard[4], Alessio Rovere[5]

[1]Institute of Earth, Ocean, and Atmospheric Sciences, Rutgers University, 71 Dudley Road, Suite 205, New Brunswick, NJ 08901, USA.
[2]Department of Earth and Planetary Sciences, Rutgers University, Piscataway, NJ, USA.
[3]Department of Geosciences, University of Massachusetts, Amherst, MA, USA.
[4]Earth and Environmental Systems Institute, Pennsylvania State University, University Park, PA, USA.
[5]MARUM, Center for Marine Environmental Sciences, University of Bremen, Germany.

Key Points:

- Improvements in Last Interglacial Antarctic mass loss estimates could appreciably reduce future sea-level rise uncertainties
- Last Interglacial sea-level constraints are increasingly informative with respect to Antarctic mass loss over 2060–2150
- If Last Interglacial sea levels were known precisely, projected 2100 Antarctic mass loss could still have uncertainties of up to ∼50 cm

Corresponding author: Daniel Gilford, daniel.gilford@rutgers.edu

Abstract

Previous studies have interpreted Last Interglacial (LIG; ∼129–116 ka) sea-level estimates in multiple different ways to calibrate projections of future Antarctic ice-sheet (AIS) mass loss and associated sea-level rise. This study systematically explores the extent to which LIG constraints could inform future Antarctic contributions to sea-level rise. We develop a Gaussian process emulator of an ice-sheet model to produce continuous probabilistic projections of Antarctic sea-level contributions over the LIG and a future high-emissions scenario. We use a Bayesian approach conditioning emulator projections on a set of LIG constraints to find associated likelihoods of model parameterizations. LIG estimates inform both the probability of past and future ice-sheet instabilities and projections of future sea-level rise through 2150. Although best-available LIG estimates do not meaningfully constrain Antarctic mass loss projections or physical processes until 2060, they become increasingly informative over the next 130 years. Uncertainties of up to 50 cm remain in future projections even if LIG Antarctic mass loss is precisely known (±5 cm), indicating there is a limit to how informative the LIG could be for ice-sheet model future projections. The efficacy of LIG constraints on Antarctic mass loss also depends on assumptions about the Greenland ice sheet and LIG sea-level chronology. However, improved field measurements and understanding of LIG sea levels still have potential to improve future sea-level projections, highlighting the importance of continued observational efforts.

1 Introduction

Coastal communities are facing increasing threats from sea-level rise, creating a growing need for comprehensive probabilistic projections (Kopp et al., 2014; Kopp, DeConto, et al., 2017; Horton et al., 2018) to inform coastal risks and adaptation practices (Buchanan et al., 2016, 2017; D. J. Rasmussen et al., 2018; Kopp et al., 2019). The single largest source of uncertainty in 21st century global-mean sea-level rise is the Antarctic ice sheet (AIS). Projected AIS mass loss depends on the ice-sheet physics considered, modeling and statistical methodologies, and observational constraints (e.g., Kopp, DeConto, et al., 2017).

There is deep uncertainty in future AIS sea-level contributions, meaning that their full probability distribution is unknown and cannot be estimated or agreed upon by experts (Lempert & Collins, 2007). The lack of expert agreement on AIS mass loss projections is partially related to unresolved challenges in modeling ice-sheet processes (Fuller et al., 2017; Bakker, Wong, et al., 2017; Bakker, Louchard, & Keller, 2017; Bamber et al., 2019). There is growing consensus that the AIS is threatened by marine ice-sheet instability (MISI; Weertman, 1974; Schoof, 2007), which would lead to accelerated mass loss irreversible on millennial timescales (Golledge et al., 2015; Bulthuis et al., 2019) and skew probability distributions towards fat upper-tails in sea-level projections (Robel et al., 2019). There is some evidence that MISI is already underway in the Thwaites/Pine Island Glacier basins (Joughin et al., 2014; Favier et al., 2014), and western AIS ice discharge has accelerated in recent years (Gardner et al., 2018; Rignot et al., 2019). Even more uncertain is the role of marine ice-cliff instability (MICI), which has recently been proposed and incorporated as a primary loss mechanism in an ice-sheet model for sea-level rise projections (Bassis & Walker, 2012; Bassis & Jacobs, 2013; Pollard et al., 2015; DeConto & Pollard, 2016).

MICI is not well understood and is difficult to parameterize. While it has not yet been observed in Antarctica, there is some modern evidence consistent with cliff instability, such as the documented calving events of Greenland glaciers (DeConto & Pollard, 2016; Parizek et al., 2019). Newly discovered iceberg-keel plough marks also provide evidence for MICI in Pine Island Bay in the early Holocene, ∼12 ka (Wise et al., 2017). However, a recent reanalysis of DeConto and Pollard (2016) showed that MICI is not well

constrained, and is unnecessary for ice-sheet model projections to be consistent with modern and paleoclimate estimates of AIS mass loss (Edwards et al., 2019). Clerc et al. (2019) examined how ice cliffs deform following removal of their buttressing ice shelves. They found that ∼90 m-tall ice cliffs would have to be lost near-instantaneously after shelf collapse to trigger MICI—on longer timescales viscous relaxation dominates the response. Furthermore, Olsen and Nettles (2019) found seismic measurements of the aforementioned Greenland glaciers were not indicative of subaerial ice cliff failure expected with MICI. These findings cannot preclude MICI as a primary mass loss mechanism in Antarctica, but they demonstrate the paucity of observations to constrain this process.

Whether or not major AIS discharge will occur through MISI and/or MICI is critical for future impacts on human systems (Oppenheimer & Alley, 2016; Wong et al., 2017; Stammer et al., 2019). But correlations between observed trends and future large-scale mass losses are weak and insignificant (Kopp, DeConto, et al., 2017), signaling that modern observations are inadequate for constraining potentially nonlinear AIS contributions to sea-level rise. Instead, the information gap must be filled with analogs from the paleo sea-level record. The Last Interglacial (LIG) period has previously been invoked to inform ice-sheet instabilities and model projections (DeConto & Pollard, 2016; Steig & Neff, 2018), but it may currently be an ineffective constraint (Edwards et al., 2019). In this study we investigate how improved estimates or different interpretations of LIG AIS mass loss may be combined with ice-sheet model ensembles to constrain probabilistic projections of future sea-level rise. We specifically choose ice-sheet model simulations which consider the MICI process to complement recent studies using similar statistical and modeling methods (DeConto & Pollard, 2016; Edwards et al., 2019).

The Last Interglacial (∼129 to 116 ka) was a period of higher orbital eccentricity, slightly warmer than present average global mean temperatures, and substantially warmer polar atmospheric temperatures (>3 K warmer than present) and high-latitude ocean temperatures (1 K warmer than present) (Capron et al., 2017, and references therein). Accompanying were estimated global mean sea levels (GMSL) about 6–9 m higher than present (Dutton, Carlson, et al., 2015), driven by a combination of mountain glacial melt, Greenland and Antarctic ice-sheet mass loss, and thermosteric effects. While the proportional mix of these contributions is uncertain, previous studies determined that some portions of the AIS retreated during the LIG (e.g., Scherer et al., 1998; Dutton, Carlson, et al., 2015; Dutton, Webster, et al., 2015). The LIG has historically been considered an analog for AIS contributions to sea-level rise in warm climates (Mercer, 1968; Hansen et al., 1981), but it may not be ideal for examining future climate change, as LIG and modern external forcing mechanisms are fundamentally different (Capron et al., 2019).

Different interpretations and applications of paleo sea-level estimates have led to divergent conclusions about what instability processes could drive future sea-level rise (cf. DeConto and Pollard (2016) and Edwards et al. (2019)). The goal of this study is to develop a framework for analyzing the extent to which the LIG could inform ice-sheet model projections of future AIS mass loss and sea-level rise. We quantify ice-sheet model projections conditioned on multiple LIG estimate distributions, and assess how narrower LIG uncertainties could improve understanding of both ice-sheet instabilities and future sea levels. We also investigate how different assumptions about LIG sea-level evolution influences ice-sheet modeling of future sea-level changes. These analyses provide useful targets and research directions for the paleo sea-level observational and ice-sheet modeling communities.

Ice-sheet models are computationally expensive to run at high resolutions necessary for sufficient accuracy. The number of simulations computationally tractable over a model's parameter space is therefore limited, making it difficult to construct an ensemble large enough to perform comprehensive statistical analyses (which are necessary for robust probabilistic projections of sea-level rise and coastal risk, e.g. Kopp, DeConto, et al., 2017; D. J. Rasmussen et al., 2020). In this study we develop a statistical "em-

ulator" designed to mimic the behavior of the ice-sheet model (the "simulator") to fill intermediate solutions that have not been simulated over the ice-sheet model parameter space (Kennedy & O'Hagan, 2001; C. E. Rasmussen & Williams, 2006; Bastos & O'Hagan, 2009). Similar to Edwards et al. (2019), we emulate ice-sheet simulations of the LIG and the future under a high-emissions scenario. The emulator provides continuous estimates of AIS sea-level contributions over two model parameters directly related to ice-sheet instability processes. We perform Bayesian statistical analyses with the emulator output to determine how the LIG constrains future Antarctic sea-level contribution projections.

Section 2 provides a detailed overview of the ice-sheet model ensembles, emulation methodology, the Bayesian approach, and LIG constraints. Our results in section 3 show how current and improved LIG estimates could constrain future Antarctic contributions to sea-level rise. We also demonstrate a specific framework application using paleo sea-level observations, and discuss our study's implications for future research directions in the paleo sea-level community. Conclusions are presented in section 4.

2 Models and Methods

2.1 Ice-sheet Model Simulations

We build ice-sheet model ensembles for the LIG and a future high-emissions scenario (Representative Concentration Pathway 8.5, RCP8.5; Riahi et al., 2011). We run simulations with the PSU Ice-sheet model, which has been used in several studies of ice-sheet contributions to past and future sea levels (Pollard & DeConto, 2009; DeConto & Pollard, 2016; Pollard et al., 2016, 2017; Kopp, DeConto, et al., 2017; Pollard et al., 2018; Edwards et al., 2019). The model (Pollard & DeConto, 2012) uses a hybrid combination of the vertically integrated shallow ice and shallow shelf approximations for ice flow (described in (Pollard & DeConto, 2012)). Ice flux at freely migrating grounding lines is parameterized (Schoof, 2007; Pollard & DeConto, 2009, 2012), while accounting for the buttressing effects of ice shelves. Hydrofracturing from surface melt and structural failure of tall ice cliffs is included (Pollard et al., 2015; DeConto & Pollard, 2016). The model simulates internal ice temperatures, with basal sliding and sediment deformation occurring only where the base is at or near the melt point, and no explicit basal hydrology. A Weertman-type basal sliding law over bedrock is used with the norm of the sliding velocity proportional to the squared norm of the basal shear stress, and spatially dependent coefficients (Pollard & DeConto, 2012). We run the model on a 10 km-resolution grid over the continental Antarctic.

Model simulations are an improvement on those of DeConto and Pollard (2016) and reanalyzed in Edwards et al. (2019). Model runs use a sub-oceanic melt scheme newly calibrated following a large ensemble analysis of model performance during the last deglaciation (Pollard et al., 2016). This improvement, developed for DeConto et al. (2020), reduces the need for a sub-surface ocean temperature bias correction on the West Antarctic margin by 50% (from 3 K to 1.5 K) relative to DeConto and Pollard (2016). Atmospheric climatologies in future simulations are also improved, as discussed below (cf. DeConto et al., 2020).

LIG equilibrium model simulations are forced by representative oceanic and atmospheric conditions from 130 ka constructed from a synthesis of paleoclimate reconstructions and climate modeling (Capron et al., 2014). We run the simulations for 5,000 years to bring them approximately into equilibrium with this fixed climate forcing; we take the final simulation values (year 5000) as representing the peak AIS mass loss response during the LIG. Emulated peak LIG mass losses are later paired with paleo sea-level estimates to assess whether the LIG could constrain future AIS contributions to sea-level rise (section 2.2–2.4).

Future transient model simulations span 1990–2150 and are reported relative to the year 2000. Following DeConto and Pollard (2016), atmospheric RCP8.5 forcing is time-interpolated and log-weighted from regional climate model Antarctic snapshots at varying levels of effective CO_2 (1×, 2×, 4×, and 8× preindustrial). Improving on DeConto and Pollard (2016), time-evolving sea-surface temperatures are synchronized in the regional atmospheric model simulations with subsurface temperatures used in the subsurface melt rate calculations, leading to favorable comparisons with an independent NCAR CESM simulation (DeConto et al., 2020, their Extended Data Figure 1).

LIG and future simulation ensembles are constructed by sampling a 2-dimensional parameter space on a regularly spaced 14×14 grid. The two parameters, CREVLIQ and CLIFVMAX (Supporting Information Table S1), are detailed in DeConto and Pollard (2016). Briefly, CREVLIQ is the proportional sensitivity of model hydrofracturing to surface liquid, i.e. from rain and meltwater ($\frac{\mathrm{m}}{(\mathrm{myr}^{-1})^2}$); it is substituted for "100" in equation (B.6) of Pollard et al. (2015). As CREVLIQ increases, ice-sheet crevasses deepen more readily with surface liquid accumulation, which increases the chance of hydrofracturing and removal of buttressing ice shelves. CLIFVMAX is the maximum rate ($\frac{\mathrm{km}}{\mathrm{yr}}$) of horizontal cliff wastage once an ice cliff becomes mechanically unstable and collapses (i.e. under MICI); it is substituted for "300" in equation (A.4) of Pollard et al. (2015) (called "VCLIF" in DeConto & Pollard, 2016). Note that when CLIFVMAX=0 $\frac{\mathrm{km}}{\mathrm{yr}}$, ice cliffs cannot retreat even when they would theoretically fail; in this set of simulations MICI is effectively turned off.

Ensembles vary CLIFVMAX and CREVLIQ over ranges of parameter values (0–13 $\frac{\mathrm{km}}{\mathrm{yr}}$ and 0–195 $\frac{\mathrm{m}}{(\mathrm{myr}^{-1})^2}$, respectively) broader than those of DeConto and Pollard (2016) and Edwards et al. (2019): the CLIFVMAX maximum is 2.6 times larger than in those studies, and the CREVLIQ range 1.3 times larger (Supporting Information Table S1). We expand the parameter value range to explore a greater range of parametric uncertainty, with upper bounds guided by observations (discussed in detail in DeConto et al., 2020) rather than the arbitrarily assigned bounds of DeConto and Pollard (2016).

Figure 1 shows ensemble timeseries of AIS mass loss in global mean sea-level equivalent from the LIG and RCP8.5 scenario; ensemble member timeseries are color-coded by CLIFVMAX values (timeseries color-coded by CREVLIQ are shown in Supporting Information Figure S1). Figure 1a includes an illustrative range of estimated LIG AIS sea-level contributions (3.1–6.1 m), which was assumed by DeConto et al. (2020) based on reconstructions described in Dutton, Carlson, et al. (2015). This LIG estimate is lower and slightly narrower than that assumed in DeConto and Pollard (2016) and Edwards et al. (2019); this and additional LIG constraints are explored below (section 2.4).

The evolution of LIG simulations (Fig. 1a) suggests that there are distinct ice-sheet mass-loss events (e.g. the accelerated mass loss in some simulations ∼1,000 years into the simulation) in response to constant forcing, depending strongly on model parameter values. This nonlinear behavior results in a multi-modal distribution of the ensemble's peak AIS mass loss (section 3). AIS discharge is sensitive to the value of CLIFVMAX on the timescale of centuries, as seen in the first 1,000 years of the LIG ensemble and the entirety of the RCP8.5 simulation (Fig. 1b). The non-monotonic color progression of timeseries in Fig. 1a suggests that CREVLIQ plays a more substantial role in ice-sheet mass loss under LIG forcing and/or on millennial timescales (Supporting Information Figures S1–S2).

Future simulations of AIS mass loss under RCP8.5 forcing are very similar across the ensemble in the early 21$^{\mathrm{st}}$ century; 158 of 196 simulations have loss rates within 1 standard deviation of IMBIE2 observed rates over 1992–2017 (15–46 $\frac{\mathrm{mm}}{\mathrm{yr}}$; IMBIE-Team, 2018). In ∼2060 ice discharge dramatically accelerates among ensemble members with higher CLIFVMAX values, and simulations markedly diverge. Across the simulations ice loss continues to accelerate through 2100 and well into the 22$^{\mathrm{nd}}$ century; 86% of the

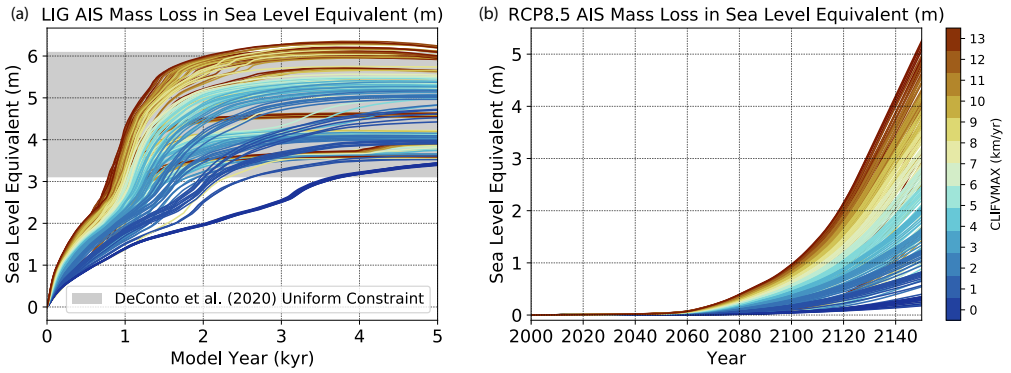


Figure 1. Timeseries of simulated AIS mass losses in sea-level equivalent (m) under (a) Last Interglacial forcing and (b) RCP8.5 forcing over 2000–2150. Simulated timeseries are color-coded by CLIFVMAX values over 0–13 $\frac{\text{km}}{\text{yr}}$. Gray shading in (a) is an illustrative range of estimated LIG AIS sea-level contributions, 3.1–6.1 m, derived in DeConto et al. (2020) and based on the reconstructions of Dutton, Carlson, et al. (2015).

simulated peak loss rates occur after 2130. By 2150, the ensemble's median rate of sea-level equivalent mass loss is 54 $\frac{\text{mm}}{\text{yr}}$, and the median AIS sea-level contribution is 2.3 m. Mean RCP8.5 ensemble AIS sea-level contributions are 42 cm in 2100 and 2.3 m in 2150. These values are lower than DeConto and Pollard (2016) large-ensemble projections (without bias corrections and with default model parameters, see their Extended Data Table 1) in both 2100 (77 cm) and 2150 (2.9 m). Differences are largely due to improved model synchronicity in atmospheric forcing, which slows the onset of surface meltwater production and ice-shelf hydrofracturing by ∼25 years compared to DeConto and Pollard (2016).

The emulator is trained only on simulations from this single ice-sheet model and with changes only in the parameters discussed above. Other ice-sheet processes or parameters that could lead to ice-sheet and ice-shelf stability or collapse have not been investigated here. Whereas our methodology is developed with a generalizable emulation and calibration framework, quantitative results in section 3 apply only to this specific ice-sheet model. The LIG could inform additional or alternative physical processes (see section 4) not considered here, and the emulation and calibration framework could be extended to include assessments of LIG constraints on the Greenland ice sheet, calibration of other ice-sheet models or ensembles (e.g. ISMIP6; Nowicki et al., 2016; Goelzer et al., 2018; Seroussi et al., 2020), calibration of different parameters or regions of parameter space, or calibration with different paleo sea-level constraints (e.g. the Pliocene).

2.2 Emulation

We train the emulator separately on LIG and RCP8.5 ensembles ($\mathbf{z}_{\text{LIG}}$ and $\mathbf{z}_{\text{RCP}}$, respectively) using Gaussian process (GP) regression (e.g. Santner et al., 2003; C. E. Rasmussen & Williams, 2006; Dubourg, 2011). We model the total AIS contributions to GMSL, $f(\theta_1, \theta_2, t)$, as the sum of two terms, each with a zero-mean GP prior distribution:

$$f(\theta_1, \theta_2, t) = f_1(\theta_1, \theta_2) + f_2(\theta_1, \theta_2, t). \tag{1}$$

The first term, $f_1(\theta_1, \theta_2)$, represents a time-independent function on the parameter space (θ_1, θ_2), and the second term, $f_2(\theta_1, \theta_2, t)$, represents the temporal evolution. We specify the prior distributions of each term as:

$$f_1(\theta_1, \theta_2) \sim \mathcal{GP}(0, \alpha_1^2 K_1(\theta_1, \theta_2, \theta_1', \theta_2'; \ell_1)), \tag{2}$$

$$f_2(\theta_1, \theta_2, t) \sim \mathcal{GP}(0, \alpha_2^2 K_2(\theta_1, \theta_2, \theta_1', \theta_2'; \ell_2) \cdot K_t(t, t'; \tau)), \tag{3}$$

where θ_1 and θ_2 are values of CLIFVMAX and CREVLIQ normalized by their respective maximum values in the simulator ensemble parameter space (Supporting Information Table S1), α_i are standard deviations, ℓ_i are characteristic length scales in the normalized parameter space, τ is a characteristic time scale and K_i are specified covariance functions. Because the LIG training data are evaluated at a single time point, there is no temporal term and f_2 is excluded from LIG GP construction. K_i are defined to be Matérn covariance functions with a specified smoothness (shape) parameter, ν, which governs how responsive the function and its realizations are to sharp changes in the training data (C. E. Rasmussen & Williams, 2006). The choice of a Matérn covariance function allows for non-parametric nonlinear behavior in time and parameter space. For the RCP8.5 scenario we set ν to $\frac{5}{2}$ because transient sea-level contributions vary smoothly over the model parameter space and time; for the LIG scenario we set ν to $\frac{1}{2}$ because peak LIG sea-level contributions vary more sharply over the model parameter space. The model form and covariance functions are chosen for a balance of simplicity, minimizing absolute errors and variance (i.e. model accuracy and precision), and maximizing the likelihood of the training data. Other covariance function and model forms were explored, but are not presented for brevity (Supporting Information Text S2).

Optimal hyperparameters (α_i, ℓ_i, and τ) of the GP models are found by maximizing the likelihoods of the training simulations (Supporting Information Table S2 C. E. Rasmussen & Williams, 2006). To ensure numerical stability we specify a "nugget" for the optimized GP representing the small-scale variability of the training data. Because the simulator is deterministic we set the nugget variance to 10^{-6} m^2, to ensure that the modeled mean approximately matches the training ensemble data across the parameter space and time. We then condition (train) the optimized GP model on the simulator ensembles ($f|\mathbf{z}$) to arrive at optimized posterior GP models for LIG and RCP8.5 which predict continuous sea-level contributions at parameter values and times between discrete training simulations. We refer the optimized posterior GPs for the LIG (f_{LIG}) and RCP8.5 (f_{RCP}) as "emulators". We perform leave-one-out analyses to validate the emulators following Bastos and O'Hagan (2009) and find they accurately mimic the behavior of the ice-sheet simulator ensembles over the LIG and RCP8.5 scenario (Supporting Information Text S1, Fig. S3–S4).

Figure 2 shows the emulator mean functions (contours) for the LIG and RCP8.5 in 2100 over the parameter space, and the corresponding training simulations (circles). There are natural similarities between the emulated sea levels during the LIG and those projected in 2100 under RCP8.5. Ice-cliff collapse and/or hydrofracturing are clearly relevant drivers of both paleo estimates and future projections by this ice-sheet model (see section 2.3): for relatively large values of CREVLIQ and CLIFVMAX, emulated AIS mass loss is likewise relatively high. Sea-level contributions are also substantially lower when either CREVLIQ or CLIFVMAX are near zero, indicating emulated sea levels with these parameter values are not appreciably influenced by either hydrofracturing from surface liquid or mechanically unstable ice-cliff retreat.

There are also differences between LIG and RCP8.5 emulator mean functions (Fig. 2, Supporting Information Figure S2). Future projected AIS mass loss is more sensitive to CLIFVMAX than CREVLIQ (cf. Fig. 1b), which becomes more pronounced throughout the early 22$^{\mathrm{nd}}$ century (not shown). Under strong RCP8.5 forcing, MICI triggers quickly,

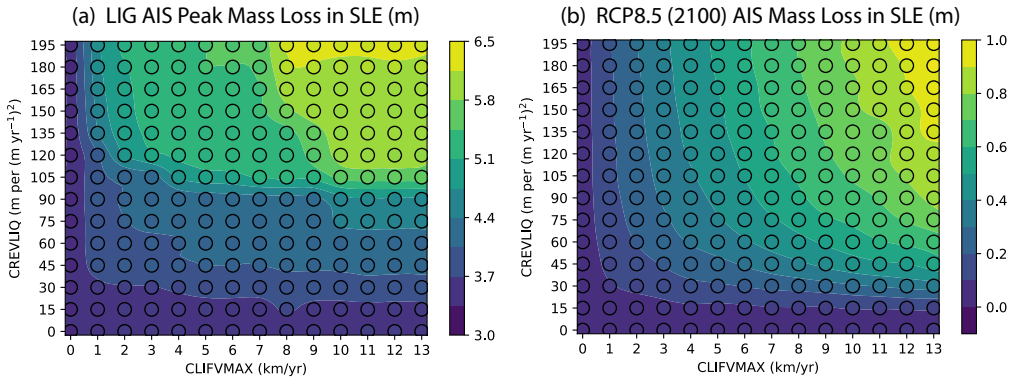


Figure 2. Simulated (filled circles) and mean emulated (contours) AIS mass losses in sea-level equivalent across ice-sheet model parameter space (a) during the Last Interglacial, and (b) projected under an RCP8.5 scenario in 2100.

and the modern ice-sheet readily loses mass at rates up to the CLIFVMAX bound. In contrast, LIG AIS sea-level contributions are more sensitive to both CREVLIQ and CLIFMVAX in some regions of the parameter space, but are nearly constant in other regions (e.g. where CREVLIQ > 120 and $2 <$ CLIFVMAX < 7, Fig. 2a). Some LIG simulations (under weaker and prolonged forcing) have discrete mass loss events that are constrained by meltwater-driven hydrofracturing (bound by CREVLIQ, cf. Supporting Information Fig. S1), making the LIG simulations generally more sensitive to CREVLIQ than the RCP8.5 simulations. Under prolonged LIG fixed forcing, different AIS sectors can be completely lost regardless of the specific parameter value in these regions of parameter space, resulting in very similar sea-level contributions. This clustering behavior is much less pronounced over the modern period of transient and increasing forcing except along fixed values of CLIFVMAX, as shown by its smoothly varying sea-level contributions (Fig. 1b and Fig. 2b). These differences across the parameter space have important implications for model calibration. In particular, they imply that even if the LIG contributions were known precisely, there may be a limit to their ability to constrain future projections. For example, the region of the parameter space with LIG contributions of ∼5.2 m (CREVLIQ > 120, $2 <$ CLIFVMAX < 7) corresponds to AIS sea-level contributions of ∼35–65 cm in 2100 under RCP8.5 forcing (Fig. 2b). This limitation is explored in detail in section 3.

Having developed emulators trained on the LIG and RCP8.5 scenario ensembles, we generate 10,000 realizations of emulator output (mean and variance, i.e. the full GP emulator) with a two-dimensional Latin-hypercube design over the parameter space. The time-dependent median and credibility intervals of the RCP8.5 emulated distribution are shown in Figure 3.

2.3 Bayesian Updating

We use a Bayesian updating approach to determine the influence of LIG constraints on future projections of Antarctic contributions to sea-level rise (e.g. Ashe et al., 2019); a glossary of relevant statistical terms is provided in Supporting Information Table S3.

There are two steps in our approach. First, we update the probability distribution of model parameters (θ_1, θ_2) based on a specified LIG constraint distribution. Applying Bayes' theorem,

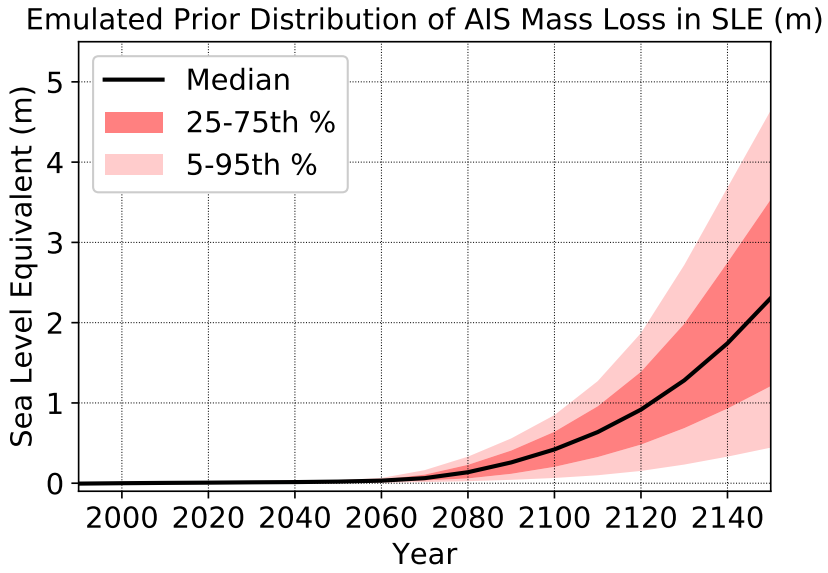


Figure 3. Emulator prior probability distribution of AIS mass loss in sea-level equivalent (m) projected under RCP8.5 forcing over 2000–2150. Shown are the median (solid black line), 25^{th}–75^{th} (dark red shading), and 5^{th}–95^{th} percentiles (light red shading) of the distribution.

$$p(\theta_1, \theta_2 \mid f_{\text{LIG}}) \propto p(f_{\text{LIG}} \mid \theta_1, \theta_2) p(\theta_1, \theta_2), \tag{4}$$

where $p(\theta_1, \theta_2 \mid f_{\text{LIG}})$ is the posterior probability of the parameters conditioned on a LIG constraint distribution, $p(f_{\text{LIG}} \mid \theta_1, \theta_2)$. This is implemented by sampling the LIG emulator with parameter values weighted by specified LIG constraints (section 2.4). $p(\theta_1, \theta_2)$ is a uniform prior probability over the input parameter space (Supporting Information Table S1). When the LIG emulator is uniformly sampled with equal likelihood across each parameter set, the emulator is not informed by any LIG constraint, and the posterior distribution mimics the underlying training simulations. We refer to this distribution of AIS mass loss as "unconstrained."

Next, to constrain future projections, we use $p(\theta_1, \theta_2 \mid f_{\text{LIG}})$ as the likelihood function of the parameters in the RCP8.5 emulator. This is represented as:

$$p(f_{\text{RCP}} \mid f_{\text{LIG}}) = p(f_{\text{RCP}} \mid \theta_1, \theta_2) p(\theta_1, \theta_2 \mid f_{\text{LIG}}), \tag{5}$$

such that the probability distribution of the constrained RCP8.5 emulator, $p(f_{\text{RCP}} \mid f_{\text{LIG}})$, is equal to the RCP8.5 emulator sampled with a uniform prior, $p(f_{\text{RCP}} \mid \theta_1, \theta_2)$ (we refer to this as the "prior" distribution), times the likelihood of the parameter values updated with a specified LIG constraint.

We demonstrate the utility of this approach in three ways. First, we explore how future projections are constrained when peak LIG AIS mass loss, x, is assumed to be precisely known (e.g. to with a 10 cm uncertainty interval). In Eqn. 4 we define the LIG constraint with a uniform distribution, $p(f_{\text{LIG}} \mid \theta_1, \theta_2) = p_x$, discretized with 10 cm-wide bins across the range of the underlying LIG simulations:

$$p_x = \mathcal{U}(x - 5\,\text{cm}, x + 5\,\text{cm}],$$

where $x = \{2.0\,\text{m}, 2.1\,\text{m}, ..., 6.9\,\text{m}, 7.0\,\text{m}\}$. The associated posteriors of RCP8.5 AIS contributions to sea-level rise, $p(f_{\text{RCP}} \mid f_{\text{LIG}})$, are a set of comprehensive time-dependent conditional probability distributions given as a function of LIG AIS mass loss. The conditional probability distributions may be integrated over a range of x values with any specified weightings, resulting in an associated constrained probability distribution of future AIS contributions to sea-level rise.

Second, we examine particular posteriors of RCP8.5 AIS contributions to sea-level rise as a function of several specific LIG constraint distributions, drawn from or adapted from the literature. Third, we analyze how the ice-sheet model projections of future AIS mass loss would be influenced through hypothetical improvements in LIG constraint distributions, either by 1) narrowing the range of uncertainty on LIG estimates, or by 2) learning that the LIG AIS sea-level contributions were relatively high (>6 m) or relatively low (<3.5 m). Each LIG constraint distribution is detailed in the following section.

2.4 LIG Constraint Distributions

We prescribe a set of LIG constraint distributions, $p(f_{\text{LIG}} \mid \theta_1, \theta_2)$, to determine the associated posterior probability distributions of future AIS contributions to sea-level rise (Eqn. 4–5). Differences between these example constraints illustrate how alternative specifications and interpretations of LIG AIS mass loss can influence projections of future sea-level rise. Figure 4a shows the probability density of each constraint distribution, along with the unconstrained LIG emulator distribution (derived by uniformly sampling the model parameter space, as discussed above).

DeConto et al. (2020) uniform distribution (**D20-U**): The uniform constraint of DeConto et al. (2020), $\mathcal{U}(3.1\text{m}, 6.1\text{m})$, is narrower and lower than that of DeConto and Pollard (2016). The primary difference is that the timing of the LIG AIS mass loss peak is assumed to peak earlier, which affects the constraint derivation; we discuss the implications of LIG sea-level chronology in detail in section 3.3. The D20-U constraint distribution is derived assuming AIS mass loss peaked in the early-LIG, concurrent with global mean sea-level estimates of 6±1.5 m from Dutton, Webster, et al. (2015). Subtracting off a small Greenland ice-sheet contribution in the early-LIG (1 m, Goelzer et al., 2016; Dahl-Jensen et al., 2013; Helsen et al., 2013) and a thermosteric rise of 0.4 m (McKay et al., 2011), and neglecting early-LIG mountain glacier melt, the residual AIS contribution is estimated as 3.1–6.1 m. Complementing the pass/fail calibration of both DeConto and Pollard (2016) and DeConto et al. (2020), we impose an analogous uniform distribution over 3.1–6.1 m, such that emulated LIG output falling within the constraint is taken as equally likely; emulator output falling outside the constraint is ascribed a probability of zero.

DeConto et al. (2020) normal distribution (**D20-N**): Whereas the uniform distribution assumes fixed limits on the LIG constraint but equal probabilities of LIG contributions between 3.1–6.1 m, it is practical to explore the implications of the central value of the estimated LIG distribution being more likely than the bounds. D20-N replaces D20-U with a Gaussian distribution—taking the central value as the mean and the bounds representing 2 standard deviations from the mean—to develop a constraint distribution following $\mathcal{N}(4.6\text{m}, (0.75\text{m})^2)$.

Edwards et al. (2019) uniform distribution (**E19-U**): The uniform distribution used to constrain the LIG Antarctic contributions in the reanalyses of Edwards et al. (2019) is identical to the calibration of DeConto and Pollard (2016) given by $\mathcal{U}(3.5\text{m}, 7.4\text{m})$. We include this constraint to specifically compare our Bayesian calibrated ensembles with the results of Edwards et al. (2019), which used a similar emulation method but employed history matching rather than Bayesian calibration of the original DeConto and Pollard (2016) ice-sheet model ensemble.

Kopp et al. (2009) time slice at 125 ka (**K09-125ka**): Kopp et al. (2009) compiled a probability distribution of AIS contributions to sea-level rise (extended by Kopp et al., 2013) by combining a comprehensive database of proxy observations of LIG sea levels, an age model, and GP regression. Posterior probability distributions of AIS LIG sea levels were estimated over time by conditioning on local sea-level and age measurements. To generate a simple constraint distribution consistent with the LIG ensemble, we take a time slice at 125 ka (5,000 years after the initial time period of forcing, 130 ka, section 2.1). This is an overly simplified interpretation of the link between the ice-sheet emulator and the posterior LIG AIS mass loss distributions, because it assumes that emulated peak LIG contributions are representative of the synthesized observational record precisely at 125 ka.

Kopp et al. (2009) maximum Antarctic contributions during the LIG (**K09-Max-3kyrSmooth**): To examine an alternative link between the ice-sheet model simulations and Kopp et al. (2009) constraints, we generate 2,500 samples from the posterior probability distribution of mean global sea level conditioned upon sea-level observations and sampled ages from Kopp et al. (2009). This represents an estimate of the distribution of the global mean sea-level maximum from the model in Kopp et al. (2009). Each sample is a realization of the evolution of AIS sea-level contributions during the LIG (between 129–114 ka). Because these samples can be noisy in time, we smooth each sample with a 3 kyr-window boxcar filter (other smoothing windows were explored, but here we focus on 3 kyr for brevity). The constraint distribution is then constructed from the peak (global maximum) Antarctic sea-level contribution of each smoothed sample (assuming each is equally likely), so that it shares an interpretation with the ice-sheet emulator (section 2.1).

We also explore two sets of hypothetical LIG constraints.

High and low distributions (**LIG AIS<3.5 m** and **LIG AIS>6 m**): We prescribe a set of hypothetical relatively high and relatively low constraints, given by $\mathcal{U}(6.0\text{m}, +\infty)$ and $\mathcal{U}(-\infty, 3.5\text{m})$, respectively. The resulting posteriors show how projections of future AIS mass loss could improve if there were a reliable upper or lower bound on LIG AIS mass loss estimates at the margins of the unconstrained LIG distribution.

Sensitivity to reduced uncertainties in LIG estimates (**Narrower D20-U**): To ascertain how future projections of AIS mass loss could be affected by reduced uncertainties in LIG constraint distributions or improved LIG estimates, we gradually reduce the range of the D20-U constraint by 10%, 25%, 50%, 75%, and 90% and assess the resulting posterior distributions; the central value (4.7 m) of each constraint is identical to that of D20-U. Physically-based observational constraints, following a similar narrowing method, are the focus of the discussion in section 3.3.

For each LIG constraint distribution, we find the associated likelihoods of the model parameters and the posterior probability distributions of projected future AIS contributions to sea-level rise following Eqn. 4–5.

An advantage of the Bayesian framework is that any specified constraint may be assessed. These constraints are not intended to be exhaustive, but rather illustrative of a range of current or potentially-improved LIG constraints and their usefulness for informing future projections.

3 Results

3.1 Conditional Probability Distributions

Figure 4b shows the conditional posterior probability densities of RCP8.5 scenario AIS mass loss in 2100 (contoured on a log-scale), assuming the LIG peak AIS sea-level

contributions were known to within 10 cm. Along each column of the horizontal axis (x values) the densities sum to one, representing the probability distributions of future AIS mass loss, $p(f_{\mathrm{RCP}} \mid f_{\mathrm{LIG}})$, in 2100 as a function of the associated 10-cm-wide uniform LIG constraint distributions, p_x (section 2.4). Conditional posterior probability densities in 2150 (Supporting Information Figure S6) have a similar structure. Figure 4b summarizes the efficacy of the Last Interglacial for informing this ice-sheet model's projections of future sea-level rise.

The posterior marginal probability distributions of CLIFVMAX and CREVLIQ show the related dependencies of model parameter likelihoods as a function of LIG constraints (Figure 5). The marginal probabilities, $p(\theta_1 \mid \theta_2, f_{LIG})$ and $p(\theta_2 \mid \theta_1, f_{LIG})$ are computed by finding the density of each model parameter as a function of the LIG constraint integrating over the other model parameter, and normalizing such that along each column of x densities sum to one. Comparison between Fig. 4b and Fig. 5 demonstrates how each LIG estimate informs projections of future AIS mass loss by constraining ice-sheet model parameters.

LIG contributions are relatively more informative on the extreme margins of the emulated probability distribution than in the interior (Fig. 4, cf. black curve of Fig. 4a). At relatively high and low ends of the unconstrained distribution, there are fewer combinations of ice-sheet model parameter values that produce these sea levels than in the interior (Fig. 5), leading to narrower posteriors in future projections. At the high end of LIG AIS mass loss (>6 m), CLIFVMAX values always exceed 7.5 $\frac{\mathrm{km}}{\mathrm{yr}}$ and CREVLIQ values are likewise relatively high (Fig. 5), suggesting MICI—driven by substantial meltwater-driven hydrofracturing and removal of buttressing ice shelves—is important for reaching high LIG losses in this model. Narrow posteriors at the low end of LIG AIS mass loss (<3.5 m) are associated emulator outputs which have little or no mass loss from MICI in this model, i.e. CLIFVMAX<1 $\frac{\mathrm{km}}{\mathrm{yr}}$ (Fig. 5). We further explore specific future projection posterior distributions associated with these relatively high and low LIG constraints in section 3.2.

Conditional RCP8.5 posterior distributions in 2100 associated with intermediate values of LIG AIS mass loss are more broad than at the margins. Even if LIG AIS mass loss were known precisely to within 10 cm, if that value was between 4 and 5.5 m then there would remain a ∼50 cm range in 2100 projections. For instance, when the LIG contribution is 4.2 m, the associated posterior 95% credible interval in 2100 is 15–65 cm. This broad range in future projections after applying a precise LIG constraint results from the contrasting sensitivities of the LIG and RCP8.5 to parameter configurations (Supporting Information Figure S2). The unconstrained LIG AIS mass loss distribution is multi-modal (Fig. 4a) indicating that different sectors of the Antarctic ice sheet have been completely lost; total mass losses in these individual modes are then insensitive to small changes in parameter values, as seen in the regions of the parameter space which have nearly constant sea-level contributions (Fig. 2a). Comparing with Fig. 5a shows there is a wide range of CLIFVMAX values which result in LIG sea-level contributions between 4 and 6 m. But RCP8.5 future AIS mass losses are most sensitive to the CLIFVMAX value when CREVLIQ>15 $\frac{\mathrm{m}}{(\mathrm{m\ yr^{-1}})^2}$ (Fig. 2), and thus have exhibit broad posterior distributions when when LIG sea-level contributions are between 4 and 6 m. LIG contributions scale gradually with CREVLIQ values until CREVLIQ>105 $\frac{\mathrm{m}}{(\mathrm{m\ yr^{-1}})^2}$, and then LIG contributions are associated with broader ranges of CREVLIQ over 105–195 $\frac{\mathrm{m}}{(\mathrm{m\ yr^{-1}})^2}$ (Fig. 5b); future AIS mass loses are relatively insensitive to CREVLIQ in this region of model parameter space (Fig. 2).

These varying responses to model parameter configurations most clearly affect RCP8.5 projections when the median in 2100 *drops* from 63 to 32 cm as LIG contributions *increase* from 4.6 to 4.8 m (Fig. 4b. This non-intuitive result suggests that in some regions of the parameter space, the model-simulated equilibrium LIG AIS mass loss is influenced by a different physical process than transient RCP8.5 losses. By 2100, RCP8.5 air tem-

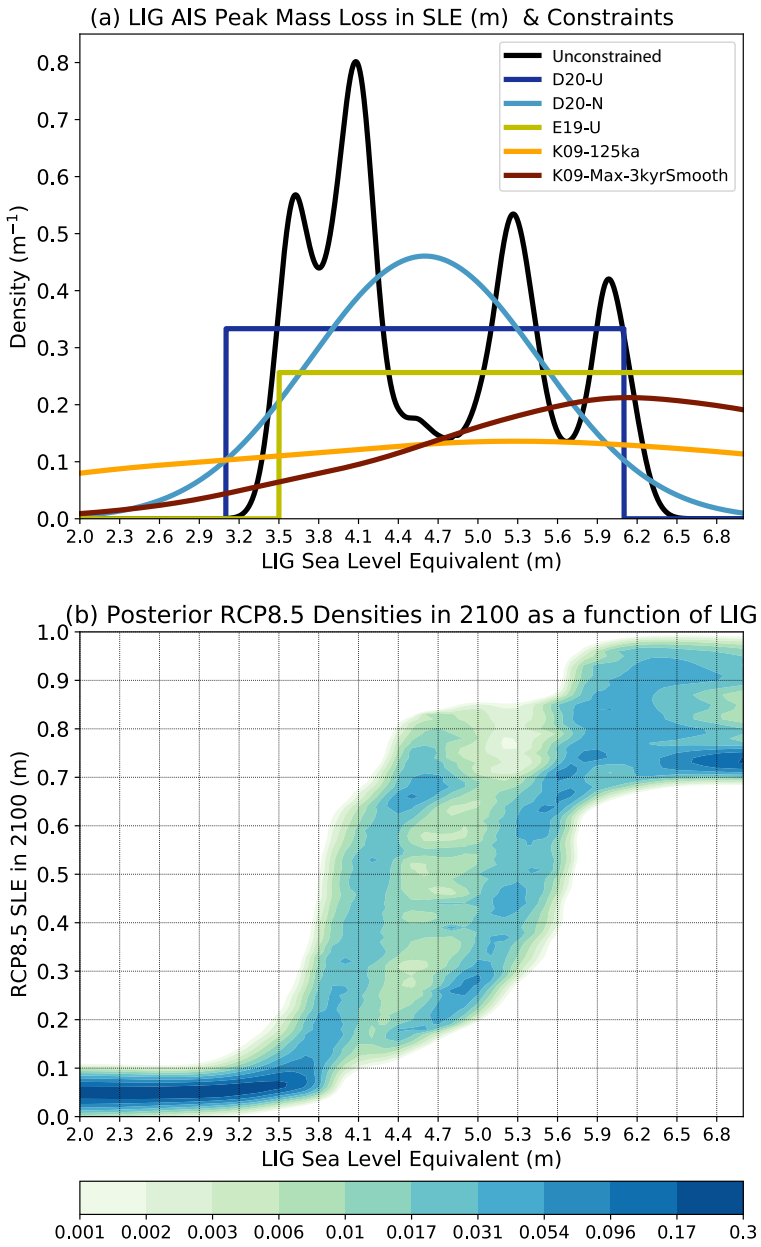


Figure 4. (a) Last Interglacial emulated unconstrained (black curve) and specified constraint (blue, yellow, orange, and red lines curves) probability distributions of Antarctic mass loss in sea-level equivalent (m). (b) Conditional posterior probability densities of Antarctic mass loss in 2100 projected under RCP8.5 forcing (in sea-level equivalent), normalized and plotted as a function of Last Interglacial AIS mass loss in sea-level equivalent (discretized with 10-cm-wide bins, see text).

perature anomalies are ∼2 K warmer than the applied LIG forcing and are still increasing, leading to accelerating AIS mass loss through MICI that is strongly influenced by CLIFVMAX. In contrast, the applied LIG forcing is cooler and fixed, and the LIG ice-sheet equilibrates by losing mass more gradually over a 5,000 period. The slower equi-

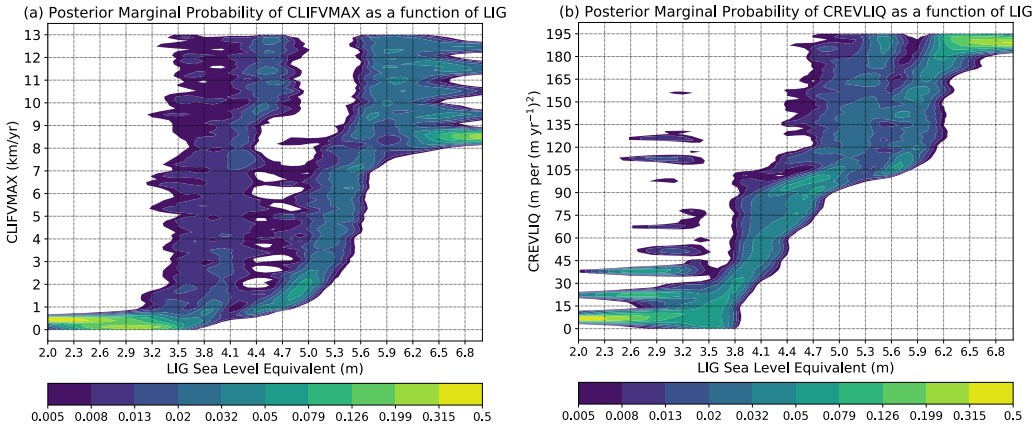


Figure 5. Posterior marginal probability distributions of (a) CLIFVMAX and (b) CREVLIQ, normalized and plotted as a function of Last Interglacial AIS mass loss in sea-level equivalent (discretized with 10-cm-wide bins, see text).

librium response permits CREVLIQ to play a larger role in LIG AIS mass loss, directing which sectors of ice eventually become unstable through shelf hydrofracturing over the prolonged period of anomalously warm temperatures (Figure 1).

Conditional posterior distributions (Fig. 4) are a powerful and novel tool for illustrating the links between ice-sheet model projections and paleo observational records. If, for instance, a field measurement showed that LIG AIS contributions were > 5 m, then the densities in Fig. 4 may be integrated across 5 m $\leq x \leq +\infty$ to show that the range of projected RCP8.5 AIS mass loss in 2100 is ∼0.2–1.0 m, with a median of 65 cm. We discuss how conditional distributions may be used in the context of particular paleo sea-level observations in section 3.3.

3.2 Future Projections Given Specific LIG Constraint Distributions

Posterior probability distributions of AIS sea-level contributions in 2100 and 2150 conditional on each LIG constraint distribution, following Eqn. (5), are shown in Figure 6, along with the emulated prior RCP8.5 distribution and histograms of the training simulations. Distributions are produced with kernel density estimation assuming a Silverman bandwidth (Silverman, 1986) reduced by 80% to prevent over-smoothing. Distribution quantiles are presented in Table 1. For reference, the likelihoods of model parameter sets—$p(\theta_1, \theta_2 \mid f_{LIG})$—associated with each LIG constraint distribution are shown in Supporting Information Figure S5.

From 1990 to 2100, specific LIG constraints (section 2.4) do not very effectively narrow uncertainties in future projections. Quantiles of the prior, D20-U, E19-U, and K09-125ka distributions in 2100 are all within 5 cm (Table 1). D20-N weights the distribution towards the lower end of the projections, dropping the 95$^{\text{th}}$ percentile (relative to the prior) by 7 cm. The K09-Max-3kyrSmooth distribution re-weights the projection distribution towards the upper tail (cf. Fig. 4a), raising the median and 75$^{\text{th}}$ percentiles by 8–10 cm.

CREVLIQ/CLIFVMAX likelihood functions (Supporting Information Figure S5) show that there is no set of parameter values which are consistently unlikely across all LIG constraints. Thus, interpretations of which regions of model parameters space are viable (and hence, deductions about the related physical processes) will depend entirely

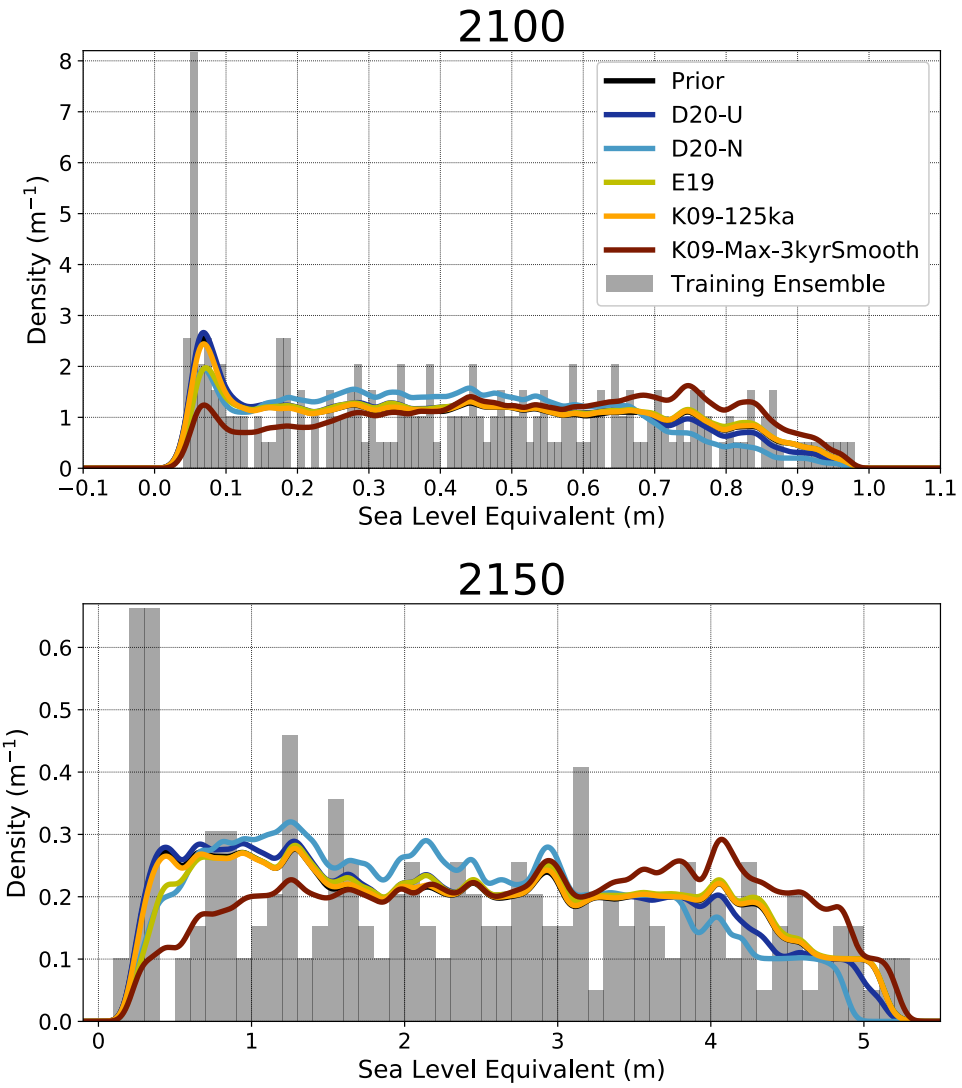


Figure 6. Projected probability distributions of Antarctic ice-sheet mass loss in sea-level equivalent (m) in (a) 2100 and (b) 2150, under RCP8.5 forcing. Distributions are from 10,000 emulator samples and smoothed with kernel density estimation. Shown are the prior RCP8.5 distribution with no constraints (black curves), and distributions under specified Last Interglacial constraints (blue, yellow, orange, and red curves, cf. Figure 4). The ice-sheet model training ensemble is plotted as a histogram scaled for comparison.

on the specific LIG constraint applied. For instance, the E19-U constraint indicates that the least likely parameter sets are where CLIFVMAX values are small (Fig. S5d): about 2.6% of the posterior density is associated with CLIFVMAX ≤ 0.5 $\frac{\text{km}}{\text{yr}}$, compared with 3.8% if the probabilities were uniformly likely in this region. This result implies that MICI is not ruled out by this constraint, in contrast to the interpretation of Edwards et al. (2019), because under E19-U CLIFVMAX ≤ 0.5 $\frac{\text{km}}{\text{yr}}$ is only a little more likely than not. As we drop to even lower values of CLIFVMAX (e.g. 0.1 $\frac{\text{km}}{\text{yr}}$), the emulated outputs conditioned on E19-U becomes less and less likely (not shown). However, there remain parameter sets with non-zero likelihoods near CLIFVMAX=0, especially at higher CREVLIQ values (Fig. S5d), such that a no-MICI solution also cannot be excluded. The main differ-

Table 1. Quantiles of projected Antarctic ice-sheet mass loss in sea-level equivalent (m) in 2100 and 2150; each emulated distribution other than the prior is constrained using a specified Last Interglacial probability distribution (section 2.4).

2100 Quantiles	Prior	D20-U	D20-N	E19-U	K09-125ka	K09-Max-3kyrSmooth
5	0.07	0.07	0.07	0.07	0.07	0.09
25	0.20	0.20	0.23	0.23	0.21	0.31
50	0.42	0.40	0.40	0.44	0.43	0.52
75	0.64	0.61	0.58	0.65	0.64	0.72
95	0.85	0.83	0.78	0.85	0.85	0.88
2150 Quantiles	Prior	D20-U	D20-N	E19-U	K09-125ka	K09-Max-3kyrSmooth
5	0.44	0.44	0.51	0.52	0.46	0.63
25	1.21	1.17	1.23	1.30	1.24	1.63
50	2.31	2.21	2.18	2.39	2.32	2.81
75	3.54	3.38	3.22	3.58	3.53	3.88
95	4.65	4.56	4.38	4.66	4.64	4.79

ences between this study and Edwards et al. (2019) are the ensemble structure, as well as enhanced atmospheric climatologies and a reduced ocean bias correction in the training simulations (section 2.1). Overall, none of the existing LIG constraints can exclude MICI as a primary loss mechanism (Fig. S5), which requires an estimated LIG AIS mass loss of less than ∼3.5 m.

The unconstrained LIG emulated distribution nearly coincides with (or in some cases is narrower than) the existing LIG constraint distributions. Whereas this indicates that the ice-sheet model is able to faithfully reproduce peak LIG AIS mass losses, it also confirms an existing challenge found by Edwards et al. (2019): current LIG estimates are not strong constraints on this ice-sheet model's parameter likelihoods and future projections.

In light of this finding, we investigate how LIG constraints *could* inform future projections of AIS mass loss and sea-level rise if they were improved, using the sensitivity test constraints outlined in section 2.4; the resulting posteriors are presented in Figure 7. In particular, LIG constraints with gradually-reduced ranges have a limit to how effective they can be for informing future projections of Antarctic contributions to sea-level rise (Supporting Information Figure S10).

Narrowing the D20-U constraint by 50% results in a posterior distribution highlighting an important property of LIG constraints: they become more effective over time (Fig. 7a). Until ∼2050 the prior and constrained distribution are nearly identical, then their distributions begin to diverge. AIS mass loss projected by this model becomes increasingly driven by cliff collapse (or the lack thereof) around 2060, and the LIG estimate begins effectively constraining both the most unstable parts of the distribution (which have the highest CLIFVMAX values, cf. Figure 1b) and the least. Figure 7a shows that because these solutions diverge over time, the LIG constraint becomes more informative on the absolute values of sea-level contributions over time. In 2100, the 95% credible interval of the posterior from the 50% narrower D20-U constraint is 14–68 cm, compared to the 7–85 cm interval of the prior (Table 1). In 2150 the constrained 95% credible interval is 0.71–4.07 m, compared with 0.44–4.65 m from the prior. Thus, even if observation-

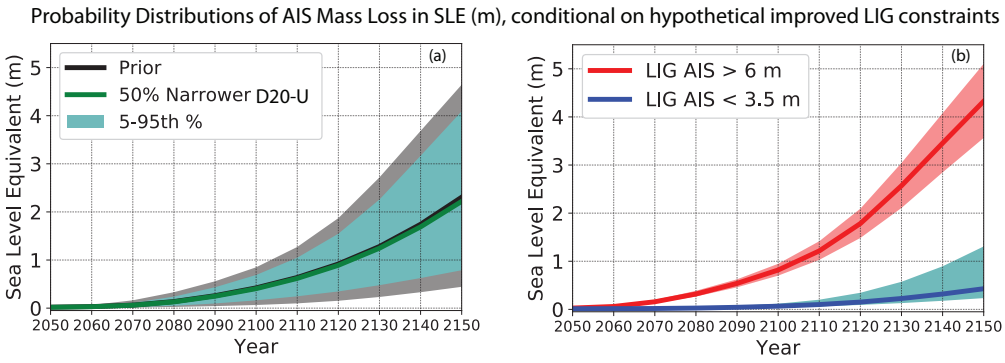


Figure 7. Posterior probability distribution medians (solid lines) and 5$^{\text{th}}$–95$^{\text{th}}$ percentiles (shading) of AIS mass loss in sea-level equivalent (m) projected under RCP8.5 forcing over 2050–2150. (a) Posterior constrained assuming the D20-U constraint was 50% narrower (green curve/shading) alongside the prior distribution reproduced from Fig. 3 (black curve/shading). (b) Posteriors constrained assuming LIG AIS sea-level contributions were <3.5 m (blue curve/shading) or >6 m (red curve/shading).

based LIG constraints are of little utility for reducing sea-level projection uncertainties in the near term, they become more meaningful as projections diverge.

We also investigate how projected AIS mass loss could change if there were a known upper or lower bound on the LIG estimate. Figure 7b shows how hypothetical estimates of relatively low (<3.5 m) or relatively high (>6 m) LIG AIS mass loss could strongly influence future projections. If the LIG contributions were known to be <3.5 m, the median and associated 95% credible interval of RCP8.5 projections in 2100 would be 7 cm and 4–15 cm, respectively. Likewise, if the LIG contributions were known to be >6 m, the associated median and 95% credible intervals of 2100 projections would be 81 cm and 68–95 cm, respectively.

A striking feature of the posterior distribution associated with LIG AIS mass loss <3.5 m constraint (blue curve/shading in Fig. 7b) is the positive skew emerging over time. Simulated ice sheets that become unstable on a reverse-sloping bed have a loss rate proportional to their grounding line thickness, and hence proportional to the amount of ice they have already lost: simulations which have lost more mass retreat faster than those which have lost less mass (Robel et al., 2019). This behavior positively skews the mass loss distribution (similarly shown by Nias et al., 2019).

Notably, interpreting the total AIS mass loss distribution is complicated by different sectors losing mass at different times and rates. As sectors of the ice sheet lose all of their mass the positive skew disappears (Robel et al., 2019), as seen in the multiple modes of the unconstrained LIG emulated distribution (Fig. 4). The bimodal positively-skewed posterior distribution associated with the 90% narrowed D20-U constraint (Fig. S10) and the weakly skewed prior distribution of RCP8.5 mass loss in 2100 (skew of +0.18, Fig. 6) also depict this complex behavior.

In contrast, the posterior distribution associated with LIG AIS <3.5 m well-illustrates how different sensitivities to instability can drive skew across an ensemble (Fig. 7b). In 2080 the emulated samples associated with higher model parameter values become unstable, and the skew increases from near zero to +1.8 by 2110; after this initial period of instability the skew remain strongly positive (> +1.3). This behavior also explains how different sensitivities to instability leads to posteriors diverging over time.

3.3 Relevance for Paleo Sea-Level Observations

We have used conditional posterior probability distributions (Fig. 4b–5) to show how the LIG informs this model's projections of AIS mass loss. Our results also show how ice-sheet model parameters are linked to estimates of LIG AIS sea-level contributions. Concurrently, any improvements in understanding physical processes in the ice-sheet will also indicate which LIG contributions are most likely. A main benefit of our approach is that it may inform future research and observational efforts to understand LIG sea levels. Here we apply our emulation and Bayesian updating framework to particular paleo sea-level observations, to investigate how assumptions about LIG ice-sheet chronology or improved LIG observations could influence future projections.

Determining sea levels during the LIG and closing its peak sea-level budget are challenging problems. Field observations have large uncertainties, related to measurement error or confounding processes such as glacial isostatic adjustment (GIA) or mantle dynamic topography (DT) (Hibbert et al., 2016; Austermann et al., 2017; Dendy et al., 2017; Rohling et al., 2017; Capron et al., 2019). Still under debate is whether the LIG exhibited variability with multiple global sea-level peaks (Kopp, Dutton, & Carlson, 2017; Barlow et al., 2018), indicating short-term fluctuations (e.g., Rohling et al., 2008), or distinct out-of-phase mass losses between the Greenland and Antarctic ice sheets (Dutton, Carlson, et al., 2015). Lacking sufficient near-field evidence, the AIS is typically invoked as an uncertain residual contributor. Yet estimated Greenland ice-sheet mass losses during the LIG also have a wide range of interpretations and central estimates (Dutton, Carlson, et al., 2015, their Figure 3), so it is difficult to disentangle the relative roles of Greenland and Antarctica.

Our method is able to show how these uncertainties in proxy-based reconstructions of LIG sea levels reflect on uncertainties in future AIS contributions to sea-level rise. Here we calculate the 95% credible intervals of AIS sea-level contributions under RCP8.5 forcing in 2100, varying the LIG AIS uncertainty according to three different scenarios for GMSL. Scenarios are derived from a milestone study by Dutton, Webster, et al. (2015), who used sea-level proxies in the Seychelles to constrain polar ice sheet mass losses during the LIG. Scenarios are developed to illustrate how individual components of uncertainty in LIG estimates contribute to projection uncertainties; thus they are not directly related to any of the holistic projections in section 2.4 (though they are most closely related to the proxy-driven estimates of the K09-Max-3kyrSmooth constraint). We note that this is a close-to-ideal case study, because Seychelles GIA and DT predictions have relatively small uncertainties. All uncertainties are 1σ and assumed to follow a normal distribution. The scenarios are:

1. Relative sea level coinciding with the highest in situ coral measured by Dutton, Webster, et al. (2015) with high-accuracy surveying techniques. The coral assemblage is interpreted as "likely intertidal" and its elevation is 8±0.2 m above modern sea level.
2. While scenario 1 is illustrative of very small uncertainties in LIG sea-level estimates, it is also incomplete because it does not account for departures from eustasy due to GIA and sea-level fingerprints. These were calculated by Dutton, Webster, et al. (2015) using model results from Dutton and Lambeck (2012) and Hay et al. (2014). Using these estimates, Dutton, Webster, et al. (2015) calculated LIG GMSL rise was 7.6±1.7 m.
3. Austermann et al. (2017) showed that mantle DT and ocean subsidence effects must be accounted for (each with large uncertainties), before GMSL can be calculated from field data. Here we use their model results for the Seychelles to illustrate how accounting for DT and ocean subsidence influences paleo GMSL estimates and their uncertainties. Subtracting ocean subsidence (-1.4 m) and DT as modelled in Austermann

et al. (2017) (-0.8±1.8m) from scenario 2, we calculate LIG GMSL rise was 9.2±2.5 m.

For each scenario, we calculate LIG AIS sea-level contributions by subtracting the contributions of the Greenland Ice Sheet (GrIS), mountain glaciers and thermal expansion following the budgetary approach of Dutton, Carlson, et al. (2015). First, we assume that the GrIS and thermosteric contributions to LIG sea level are known (2 m and 1 m, respectively), with no error. We compare with the assumption that, instead, GrIS contributed 2 m±1.5 m to LIG GMSL, as shown in Dutton, Carlson, et al. (2015, Figure 3). We set the contributions from mountain glaciers and thermosteric expansion to 1 m (Dutton, Carlson, et al., 2015), with arbitrary uncertainties of ±0.2 m.

This exercise (Figure 8A–C) shows that, regardless of AIS mass loss during the LIG, any LIG constraint can only substantially reduce uncertainties in this ice-sheet model's projected AIS sea-level contributions if the following two conditions are met: 1) sea-level data and departures from eustasy are known with $\pm 1\sigma$ uncertainties of a few decimeters and 2) GrIS and thermal expansion uncertainties are small (<1 m). Constraints on other models could be stronger or weaker, depending on the particular relationship between their parameters and ice-sheet evolution. This could be considered discouraging for the communities working on these topics, i.e. the large intrinsic uncertainties that characterize GrIS and proxy-based ESL estimates may seem insurmountable. We instead note that this knowledge gap provides a unique opportunity to do innovative, timely and important research that feeds directly into the open research questions in the paleo sea-level and ice-sheet communities (Capron et al., 2019).

Results further suggest that the storyline of LIG sea-level evolution has a strong influence on whether the LIG is able to constrain future sea-level changes. Greenland and Antarctic sea-level contributions are inextricably linked during the LIG: knowledge or evidence about one will inform the other, as shown by assuming LIG total GMSL estimates of 7.5±0.5 m in Figure 8D. Resulting relatively high or low AIS estimates are similar to the hypothetical constraint posteriors in Fig. 7b. The links between the ice sheets imply that 1) efforts to improve estimates of GrIS can directly inform future AIS sea-level projections, and that 2) the timing of LIG GrIS loss compared with LIG AIS loss is pivotal (Kopp, Dutton, & Carlson, 2017). Storylines where GrIS and AIS mass losses peak simultaneously have a very different interpretation from those where ice-sheet losses peak several thousand years apart (Rohling et al., 2019) and imply different AIS projected contributions to future sea-level rise.

The mismatch between transient future ice-sheet mass loss and peak LIG mass loss limits the effectiveness of the LIG as a constraint. Historically, studies of the LIG have focused primarily on gathering geological evidence of peak LIG GMSL, in part because these are less challenging measurements to make in the field. But comparing the modeled LIG and future timeseries in Fig. 1 shows the transient onset of LIG losses most closely mirrors future losses, with similar dependencies on model physics and parameters. Both improved transient (rather than equilibrium) ice-sheet model runs and quality estimates of the LIG onset period are highly desirable for constraining AIS changes and future sea-level rise. Sampling biases and the requirement for precise chronologies have to this point thwarted these efforts. But as a coherent picture of LIG sea levels emerges, combining LIG constraints with probabilistic distributions from ice-sheet models—as this study has done—will improve the precision of future sea-level projections.

4 Summary and Conclusions

This study applied Bayesian methods to emulate and calibrate an ice-sheet model to evaluate the ability of LIG AIS mass loss to constrain sea-level rise projections under RCP8.5 forcing. Ice-sheet model training ensembles were developed considering the

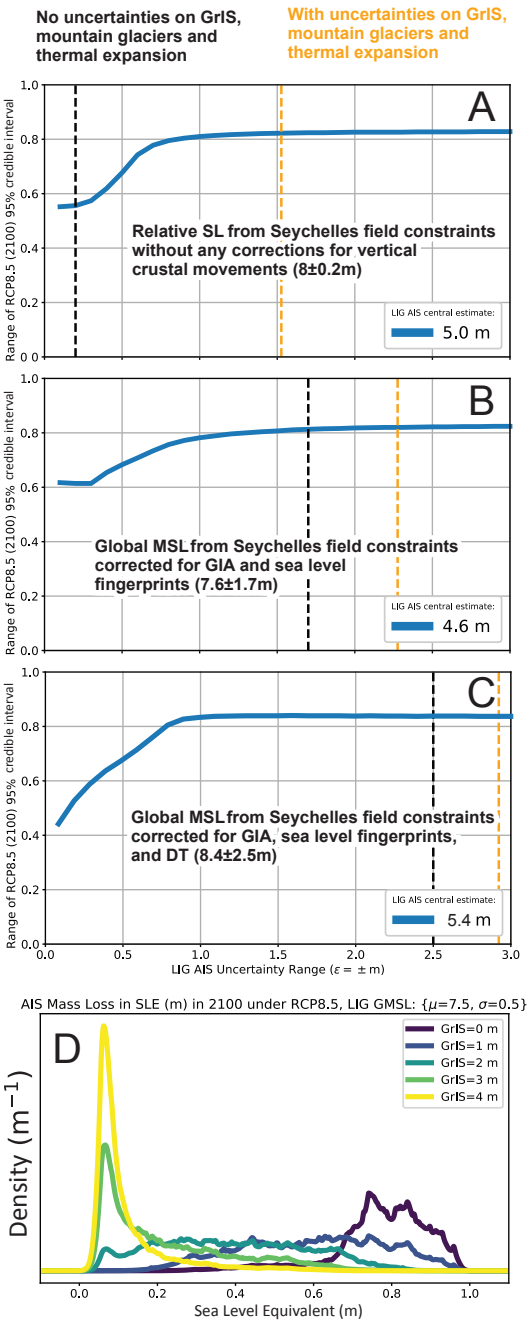


Figure 8. (A–C) Range of 95% credible intervals of future AIS sea-level contributions in 2100 under RCP8.5 forcing (m) conditional on three scenarios of LIG AIS contributions with a central estimate (blue curves) and Gaussian 1σ uncertainties (see text); combined total GrIS and thermosteric mean contributions are taken to be 3 m. Black dashed curves show the total field uncertainties excluding those from GrIS and thermosteric contributions; orange dashed curves include GrIS and thermosteric uncertainties. (D) Probability density functions of AIS contributions in 2100 under RCP8.5 forcing, conditional on LIG global mean sea levels of 7.5±0.5 m, and mean GrIS sea-level contributions varying over 0–4 m.

marine ice-cliff instability (MICI) process, with ensembles spanning over a broader range of model parameter values than previously explored (DeConto & Pollard, 2016). A set of proposed specific LIG constraint distributions (several of which have been previously used to calibrate ice-sheet model projections) were also employed to explore their effectiveness for constraining future AIS mass loss. The emulator was combined with LIG paleo sea level field measurements to illustrate how improved LIG observational estimates could potentially narrow uncertainties in future Antarctic ice-sheet projections.

Results explicitly show how estimates of LIG AIS mass loss could inform which parameter values are most likely in this ice-sheet model, which in turn informs future projections (2000–2150). However, LIG AIS sea-level contributions themselves are not well constrained (e.g., Düsterhus et al., 2016), and not all LIG estimates inform future projections equally. For instance, if LIG contributions were known to be <4 m, then MICI is very unlikely to be a primary loss mechanism in the future Antarctic mass loss projected by this ice-sheet model. Likewise, if LIG contributions were known to be >6 m, the ice-sheet model emulator projects that substantial future mass losses associated with MICI are likely. In either case, uncertainties in future projections from this model would narrow considerably, but some uncertainty would remain because peak LIG Antarctic mass losses have somewhat different sensitivities to ice-sheet model parameters than future changes do. LIG observations which inform the upper and lower limits of the unconstrained probability distribution would be valuable for improving future projections (in the context of this specific model and ensemble). Because ice-sheet model parameter likelihoods and LIG sea-level estimates are closely linked, evidence of constraints on one informs the other. For instance, if there are indications that MICI is not a viable loss mechanism, results here indicate that peak LIG Antarctic sea-level contributions were likely <4 m.

Consistent with the findings of Edwards et al. (2019), posterior distributions calibrated with a Bayesian approach show that currently best-available LIG constraints (which have previously used to calibrate ice-sheet model projections, e.g., DeConto & Pollard, 2016; Edwards et al., 2019) are inadequate to restrict a wide range of model parameter values. Consequently, this study can neither confirm nor exclude MICI as a primary driver of AIS mass loss. However, because the ice-sheet model projections of future AIS mass loss diverge over time—especially after 2060 when MICI begins strongly accelerating mass loss—LIG constraints which are uninformative in the near term become more informative on longer time scales (through 2150).

Conditioning future AIS mass losses on peak LIG sea level exposes direct links between paleo sea-level reconstructions and future sea-level rise. Improvements in field measurements, reductions in uncertainties from glacial isostatic adjustment or dynamic topography, and better chronologies of Antarctic and Greenland ice-sheet retreat during the LIG could all reduce uncertainties in future projections. These results provide strong motivation and support for continued collaborations between the paleo sea level and ice-sheet communities.

Past studies of LIG sea level have focused primarily on peak global mean sea levels, as they are more readily and reliably measurable, and because it is difficult to establish accurate and precise sea-level chronologies (Dutton, Carlson, et al., 2015). But peak LIG Antarctic ice-sheet mass losses are not necessarily representative of the transient changes the Antarctic ice-sheet may experience in the coming decades and centuries. This mismatch between the future and the past limits the applicability of LIG constraints on future Antarctic mass loss. Even if LIG Antarctic contributions were known precisely (±5 cm), there would still be decimeter-scale uncertainties in projections of future Antarctic contributions to sea-level rise. An alternative approach could be to pursue additional field observations detailing or inferring Antarctic changes during the LIG onset, to provide improved constraints on projections of future AIS contributions to sea-level rise. Im-

proved LIG chronologies and observations of LIG Greenland ice-sheet changes could also reduce future projection uncertainties.

This study considered a single ice-sheet model and explored the MICI process. Other parameterized processes (such as the oceanic melt factor or the timescale of isostatic rebound; e.g. Chang et al., 2016; Pollard et al., 2016) are well-suited for exploration with the methodological approach developed here. It should be noted that expanding on the number or range of parameters is limited by the computational efficiency of Gaussian process modeling, which scales with n samples as $\mathcal{O}(n^3)$ (C. E. Rasmussen & Williams, 2006). Alternative sampling techniques (such as such as a Latin Hypercube or Sobol sequence) could be utilized to improve efficiency on our factorial scheme. Other considerations—such as the Last Interglacial forcing applied, future emissions scenarios, or underlying stochastic processes like basal sliding—also contribute to uncertainties which are beyond the scope of this work, but with simplifications or extensions could be explored with an an approach similar to this study.

There is a maximum possible constraint that the LIG can provide to inform ice-sheet model sensitivities to climate warming and future sea-level rise (e.g., Capron et al., 2019, and references therein). Uncertainties in ice-sheet physics and observational evidence currently limit the capability of the LIG to meaningfully constrain sea-level rise projections over the coming century. Despite these limitations, this study has specifically illustrated how models, emulation, and Bayesian calibration may be combined to interpret and guide paleo sea-level observational constraints. A major ongoing research objective is to continue strategically gathering field observations, in order to improve understanding and estimates of LIG sea levels. Such improvements, along with continued integration with modeling and statistical methods, will increase confidence in the physics and projections of Antarctic contributions to sea-level rise over the coming centuries.

Acknowledgments

We thank Andrea Dutton, Anna Ruth Halberstadt, Jacky Austermann, three anonymous reviewers, and the editors for helpful comments which improved this manuscript. DG, RK, RD, and DP were supported by NSF Grant ICER-1663807 and NASA Grant 80NSSC17K0698. EA and RK were supported by NSF Grant OCE-1702587. AR is supported by the European Research Council, under the European Union's Horizon 2020 research and innovation programme (grant agreement n. 802414). This paper grew, in part, out of discussions at the 2018 PALeo constraints on SEA level rise (PALSEA) annual meeting (see Capron et al., 2019). PALSEA is a working group of the International Union for Quaternary Sciences (INQUA) and Past Global Changes (PAGES), which in turn received support from the Swiss Academy of Sciences and the Chinese Academy of Sciences. Model simulations used in this study are freely available at `https://doi.org/10.5281/zenodo.3478486`. Code to perform these analyses will be available upon publication. GP regression was performed with GPflow version 1.3.0 (Matthews et al., 2017); some colormaps provided by Crameri (2018).

References

Ashe, E. L., Cahill, N., Hay, C., Khan, N. S., Kemp, A., Engelhart, S. E., ... Kopp, R. E. (2019). Statistical modeling of rates and trends in holocene relative sea level. *Quaternary Science Reviews*, *204*, 58 - 77. Retrieved from `http://www.sciencedirect.com/science/article/pii/S0277379118302130` doi: https://doi.org/10.1016/j.quascirev.2018.10.032

Austermann, J., Mitrovica, J. X., Huybers, P., & Rovere, A. (2017). Detection of a dynamic topography signal in last interglacial sea-level records. *Science Advances*, *3*(7), 2017–13646. Retrieved from `https://meetingorganizer.copernicus.org/EGU2017/EGU2017-13646.pdf` doi:

10.1126/sciadv.1700457

Bakker, A. M., Louchard, D., & Keller, K. (2017). Sources and implications of deep uncertainties surrounding sea-level projections. *Climatic Change*, *140*(3-4), 339–347. Retrieved from http://dx.doi.org/10.1007/s10584-016-1864-1 doi: 10.1007/s10584-016-1864-1

Bakker, A. M., Wong, T. E., Ruckert, K. L., & Keller, K. (2017). Sea-level projections representing the deeply uncertain contribution of the West Antarctic ice sheet. *Scientific Reports*, *7*(1), 1–7. doi: 10.1038/s41598-017-04134-5

Bamber, J. J. L., Oppenheimer, M., Kopp, R. E., Aspinall, W. P., & Cooke, R. M. (2019). Ice sheet contributions to future sea-level rise from structured expert judgement. *Proceedings of the National Academy of Sciences*, *in review*, 1–6. doi: 10.1073/pnas.1817205116

Barlow, N. L., McClymont, E. L., Whitehouse, P. L., Stokes, C. R., Jamieson, S. S., Woodroffe, S. A., ... Sanchez-Montes, M. L. (2018). Lack of evidence for a substantial sea-level fluctuation within the Last Interglacial. *Nature Geoscience*, *11*(9), 627–634. Retrieved from http://dx.doi.org/10.1038/s41561-018-0195-4 doi: 10.1038/s41561-018-0195-4

Bassis, J. N., & Jacobs, S. (2013). Diverse calving patterns linked to glacier geometry. *Nature Geoscience*, *6*(10), 833–836. doi: 10.1038/ngeo1887

Bassis, J. N., & Walker, C. C. (2012). Upper and lower limits on the stability of calving glaciers from the yield strength envelope of ice. *Proceedings of the Royal Society A: Mathematical, Physical and Engineering Sciences*, *468*(2140), 913–931. doi: 10.1098/rspa.2011.0422

Bastos, L. S., & O'Hagan, A. (2009). Diagnostics for gaussian process emulators. *Technometrics*, *51*(4), 425–438. doi: 10.1198/TECH.2009.08019

Buchanan, M. K., Kopp, R. E., Oppenheimer, M., & Tebaldi, C. (2016). Allowances for evolving coastal flood risk under uncertain local sea-level rise. *Climatic Change*, *137*(3-4), 347–362. Retrieved from http://dx.doi.org/10.1007/s10584-016-1664-7 doi: 10.1007/s10584-016-1664-7

Buchanan, M. K., Oppenheimer, M., & Kopp, R. E. (2017). Amplification of flood frequencies with local sea level rise and emerging flood regimes. *Environmental Research Letters*, *12*(6). doi: 10.1088/1748-9326/aa6cb3

Bulthuis, K., Arnst, M., Sun, S., & Pattyn, F. (2019). *Uncertainty quantification of the multi-centennial response of the Antarctic Ice Sheet to climate change.* doi: 10.5194/tc-2018-220

Capron, E., Govin, A., Feng, R., Otto-Bliesner, B. L., & Wolff, E. W. (2017). Critical evaluation of climate syntheses to benchmark CMIP6/PMIP4 127 ka Last Interglacial simulations in the high-latitude regions. *Quaternary Science Reviews*, *168*, 137–150. Retrieved from https://doi.org/10.1016/j.quascirev.2017.04.019 doi: 10.1016/j.quascirev.2017.04.019

Capron, E., Govin, A., Stone, E. J., Masson-Delmotte, V., Mulitza, S., Otto-Bliesner, B., ... Wolff, E. W. (2014). Temporal and spatial structure of multi-millennial temperature changes at high latitudes during the Last interglacial. *Quaternary Science Reviews*, *103*, 116–133. doi: 10.1016/j.quascirev.2014.08.018

Capron, E., Rovere, A., Austermann, J., Axford, Y., Barlow, N. L., Carlson, A. E., ... Wolff, E. W. (2019). *Challenges and research priorities to understand interactions between climate, ice sheets and global mean sea level during past interglacials.* Retrieved from https://linkinghub.elsevier.com/retrieve/pii/S0277379119305207 doi: 10.1016/j.quascirev.2019.06.030

Chang, W., Haran, M., Applegate, P., & Pollard, D. (2016). Calibrating an ice sheet model using high-dimensional binary spatial data. *Journal of the American Statistical Association*, *111*(513), 57-72. Retrieved from https://doi.org/10.1080/01621459.2015.1108199 doi: 10.1080/01621459.2015.1108199

Clerc, F., Minchew, B. M., & Behn, M. D. (2019). Marine Ice Cliff Instability Mit-

igated by Slow Removal of Ice Shelves. *Geophysical Research Letters*, *46*(21), 12108–12116. doi: 10.1029/2019GL084183

Crameri, F. (2018). Geodynamic diagnostics, scientific visualisation and staglab 3.0. *Geoscientific Model Development*, *11*(6), 2541–2562. Retrieved from https://www.geosci-model-dev.net/11/2541/2018/ doi: 10.5194/gmd-11-2541-2018

Dahl-Jensen, D., Albert, M. R., Aldahan, A. A., Azuma, N., Balslev-Clausen, D., Baumgartner, M. R., ... Community, N. (2013). Eemian interglacial reconstructed from a greenland folded ice core. *Nature*, *493*, 489-494.

DeConto, R. M., & Pollard, D. (2016). Contribution of Antarctica to past and future sea-level rise. *Nature*, *531*(7596), 591–597. Retrieved from http://dx.doi.org/10.1038/nature17145 doi: 10.1038/nature17145

DeConto, R. M., Pollard, D., Alley, R. B., Velicogna, I., Gasson, E., Gomez, N., ... Kopp, R. E. (2020). The Paris Climate Agreement and future sea level rise from Antarctica. *Nature, under review May 2020*.

Dendy, S., Austermann, J., Creveling, J. R., & Mitrovica, J. X. (2017). Sensitivity of Last Interglacial sea-level high stands to ice sheet configuration during Marine Isotope Stage 6. *Quaternary Science Reviews*, *171*, 234–244. Retrieved from http://dx.doi.org/10.1016/j.quascirev.2017.06.013 doi: 10.1016/j.quascirev.2017.06.013

Dubourg, V. (2011). *Adaptive surrogate models for reliability analysis and reliability-based design optimization* (Unpublished doctoral dissertation). Universite Blaise Pascal – Clermont II.

Düsterhus, A., Tamisiea, M. E., & Jevrejeva, S. (2016). Estimating the sea level highstand during the last interglacial: A probabilistic massive ensemble approach. *Geophysical Journal International*, *206*(2), 900–920. doi: 10.1093/gji/ggw174

Dutton, A., Carlson, A. E., Long, A. J., Milne, G. A., Clark, P. U., DeConto, R., ... Raymo, M. E. (2015). Sea-level rise due to polar ice-sheet mass loss during past warm periods. *Science*, *349*(6244). doi: 10.1126/science.aaa4019

Dutton, A., & Lambeck, K. (2012). Ice volume and sea level during the last interglacial. *Science*, *337*(6091), 216–219. doi: 10.1126/science.1205749

Dutton, A., Webster, J. M., Zwartz, D., Lambeck, K., & Wohlfarth, B. (2015). Tropical tales of polar ice: Evidence of Last Interglacial polar ice sheet retreat recorded by fossil reefs of the granitic Seychelles islands. *Quaternary Science Reviews*, *107*, 182e196–196. Retrieved from http://dx.doi.org/10.1016/j.quascirev.2014.10.025 doi: 10.1016/j.quascirev.2014.10.025

Edwards, T. L., Brandon, M., Durand, G., Edwards, N. R., Golledge, N. R., Holden, P. B., ... Ritz, C. (2019). Revisiting Antarctic ice loss due to marine ice cliff instability. *Nature*, 1–35. Retrieved from http://dx.doi.org/10.1038/s41586-019-0901-4 doi: 10.1038/s41586-019-0901-4

Favier, L., Durand, G., Cornford, S. L., Gudmundsson, G. H., Gagliardini, O., Gillet-Chaulet, F., ... Le Brocq, A. M. (2014). Retreat of Pine Island Glacier controlled by marine ice-sheet instability. *Nature Climate Change*, *4*(2), 117–121. Retrieved from http://dx.doi.org/10.1038/nclimate2094 doi: 10.1038/nclimate2094

Fuller, R. W., Wong, T. E., & Keller, K. (2017). Probabilistic inversion of expert assessments to inform projections about Antarctic ice sheet responses. , 6–9.

Gardner, A. S., Moholdt, G., Scambos, T., Fahnstock, M., Ligtenberg, S., Van Den Broeke, M., & Nilsson, J. (2018). Increased West Antarctic and unchanged East Antarctic ice discharge over the last 7 years. *Cryosphere*, *12*(2), 521–547. doi: 10.5194/tc-12-521-2018

Goelzer, H., Huybrechts, P., Marie-France, L., & Fichefet, T. (2016). Last Interglacial climate and sea-level evolution from a coupled ice sheet-climate model. *Climate of the Past*, *12*(12), 2195–2213. doi: 10.5194/cp-12-2195-2016

Goelzer, H., Nowicki, S., Edwards, T., Beckley, M., Abe-Ouchi, A., Aschwanden, A., ... Ziemen, F. A. (2018). Design and results of the ice sheet model initialisation initMIP-Greenland: An ISMIP6 intercomparison. *Cryosphere*, *12*(4), 1433–1460. doi: 10.5194/tc-12-1433-2018

Golledge, N. R., Kowalewski, D. E., Naish, T. R., Levy, R. H., Fogwill, C. J., & Gasson, E. G. (2015). The multi-millennial Antarctic commitment to future sea-level rise. *Nature*, *526*(7573), 421–425. doi: 10.1038/nature15706

Hansen, J., Johnson, D., Lacis, A., Lebedeff, S., Lee, P., Rind, D., & Russell, G. (1981). Climate impact of increasing atmospheric carbon dioxide. *Science*, *213*(4511), 957–966. doi: 10.1126/science.213.4511.957

Hay, C., Mitrovica, J. X., Gomez, N., Creveling, J. R., Austermann, J., & Kopp, R. R. (2014). The sea-level fingerprints of ice-sheet collapse during interglacial periods. *Quaternary Science Reviews*, *87*, 60–69. Retrieved from `http://dx.doi.org/10.1016/j.quascirev.2013.12.022` doi: 10.1016/j.quascirev.2013.12.022

Helsen, M. M., van de Berg, W. J., van de Wal, R. S. W., van den Broeke, M. R., & Oerlemans, J. (2013). Coupled regional climatendash;ice-sheet simulation shows limited greenland ice loss during the eemian. *Climate of the Past*, *9*(4), 1773–1788. Retrieved from `https://www.clim-past.net/9/1773/2013/` doi: 10.5194/cp-9-1773-2013

Hibbert, F. D., Rohling, E. J., Dutton, A., Williams, F. H., Chutcharavan, P. M., Zhao, C., & Tamisiea, M. E. (2016). Coral indicators of past sea-level change: A global repository of U-series dated benchmarks. *Quaternary Science Reviews*, *145*, 1–56. Retrieved from `http://dx.doi.org/10.1016/j.quascirev.2016.04.019` doi: 10.1016/j.quascirev.2016.04.019

Horton, B. P., Kopp, R. E., Garner, A. J., Carling, C., Khan, N. S., Roy, K., & Shaw, T. A. (2018). Mapping sea-level change in time, space and probability. *Annual Reviews of Energy and the Environment*, *in review*(July), 1–41.

IMBIE-Team. (2018). Mass balance of the Antarctic ice sheet from 1992 to 2017. *Nature*, *558*, 219–222. doi: 10.1098/rsta.2006.1792

Joughin, I., Smith, B. E., & Medley, B. (2014). Marine ice sheet collapse potentially under way for the thwaites glacier basin, West Antarctica. *Science*, *344*(6185), 735–738. doi: 10.1126/science.1249055

Kennedy, M. C., & O'Hagan, A. (2001). Bayesian calibration of computer models. *Journal of the Royal Statistical Society: Series B (Statistical Methodology)*, *63*(3), 425–464. Retrieved from `http://doi.wiley.com/10.1111/1467-9868.00294` doi: 10.1111/1467-9868.00294

Kopp, R. E., DeConto, R. M., Bader, D. A., Hay, C. C., Horton, R. M., Kulp, S., ... Strauss, B. H. (2017). Evolving Understanding of Antarctic Ice-Sheet Physics and Ambiguity in Probabilistic Sea-Level Projections. *Earth's Future*, *5*(12), 1217–1233. doi: 10.1002/2017EF000663

Kopp, R. E., Dutton, A., & Carlson, A. (2017). Centennial- to millennial-scale sea-level change during the Holocene and Last Interglacial periods. *Past Global Changes Magazine*, *25*(3), 148–149. doi: 10.22498/pages.25.3.148

Kopp, R. E., Gilmore, E. A., Little, C. M., Lorenzo-Trueba, J., Ramenzoni, V. C., & Sweet, W. V. (2019). Usable science for managing the risks of sea-level rise. *Earth's Future*, *7*(12), 1235-1269. Retrieved from `https://agupubs.onlinelibrary.wiley.com/doi/abs/10.1029/2018EF001145` doi: 10.1029/2018EF001145

Kopp, R. E., Horton, R. M., Little, C. M., Mitrovica, J. X., Oppenheimer, M., Rasmussen, D. J., ... Tebaldi, C. (2014). Probabilistic 21st and 22nd century sea-level projections at a global network of tide-gauge sites. *Earth's Future*, *2*(8), 383–406. Retrieved from `http://doi.wiley.com/10.1002/2014EF000239` doi: 10.1002/2014EF000239

Kopp, R. E., Simons, F. J., Mitrovica, J. X., Maloof, A. C., & Oppenheimer, M.

(2009). Probabilistic assessment of sea level during the last interglacial stage. *Nature*, *462*(7275), 863–867. Retrieved from http://dx.doi.org/10.1038/nature08686 doi: 10.1038/nature08686

Kopp, R. E., Simons, F. J., Mitrovica, J. X., Maloof, A. C., & Oppenheimer, M. (2013). A probabilistic assessment of sea level variations within the last interglacial stage. *Geophysical Journal International*, *193*(2), 711–716. doi: 10.1093/gji/ggt029

Lempert, R. J., & Collins, M. T. (2007). Managing the risk of uncertain threshold responses: Comparison of robust, optimum, and precautionary approaches. *Risk Analysis*, *27*(4), 1009–1026. doi: 10.1111/j.1539-6924.2007.00940.x

Matthews, A. G. d. G., van der Wilk, M., Nickson, T., Fujii, K., Boukouvalas, A., Le'on-Villagr'a, P., ... Hensman, J. (2017, apr). GPflow: A Gaussian process library using TensorFlow. *Journal of Machine Learning Research*, *18*(40), 1-6. Retrieved from http://jmlr.org/papers/v18/16-537.html

McKay, N. P., Overpeck, J. T., & Otto-Bliesner, B. L. (2011). The role of ocean thermal expansion in Last Interglacial sea level rise. *Geophysical Research Letters*, *38*(14), 4–9. doi: 10.1029/2011GL048280

Mercer, J. H. (1968). Antarctic ice and Sangamon sea level. *International Association of Scientific Hydrology*, *79*(139), 217–225. Retrieved from https://iahs.info/uploads/dms/079020.pdf

Nias, I. J., Cornford, S. L., Edwards, T. L., Gourmelen, N., & Payne, A. J. (2019). Assessing Uncertainty in the Dynamical Ice Response to Ocean Warming in the Amundsen Sea Embayment, West Antarctica. *Geophysical Research Letters*, *46*(20), 11253–11260. doi: 10.1029/2019GL084941

Nowicki, S. M., Payne, A., Larour, E., Seroussi, H., Goelzer, H., Lipscomb, W., ... Shepherd, A. (2016). Ice Sheet Model Intercomparison Project (ISMIP6) contribution to CMIP6. *Geoscientific Model Development*, *9*(12), 4521–4545. doi: 10.5194/gmd-9-4521-2016

Olsen, K. G., & Nettles, M. (2019). Constraints on Terminus Dynamics at Greenland Glaciers From Small Glacial Earthquakes. *Journal of Geophysical Research: Earth Surface*, *124*(7), 1899–1918. doi: 10.1029/2019JF005054

Oppenheimer, M., & Alley, R. B. (2016). How high will the seas rise? *Science*, *354*(6318), 1375–1377. doi: 10.1126/science.aak9460

Parizek, B. R., Christianson, K., Alley, R. B., Voytenko, D., Vaňková, I., Dixon, T. H., ... Holland, D. M. (2019). Ice-cliff failure via retrogressive slumping. *Geology*, *47*(5), 449–452. doi: 10.1130/G45880.1

Pollard, D., Chang, W., Haran, M., Applegate, P., & DeConto, R. (2016). Large ensemble modeling of the last deglacial retreat of the West Antarctic Ice Sheet: Comparison of simple and advanced statistical techniques. *Geoscientific Model Development*, *9*(5), 1697–1723. doi: 10.5194/gmd-9-1697-2016

Pollard, D., & DeConto, R. M. (2009). Modelling West Antarctic ice sheet growth and collapse through the past five million years. *Nature*, *458*(7236), 329–332. Retrieved from http://dx.doi.org/10.1038/nature07809 doi: 10.1038/nature07809

Pollard, D., & DeConto, R. M. (2012). Description of a hybrid ice sheet-shelf model, and application to Antarctica. *Geoscientific Model Development*, *5*(5), 1273–1295. doi: 10.5194/gmd-5-1273-2012

Pollard, D., DeConto, R. M., & Alley, R. B. (2015). Potential Antarctic Ice Sheet retreat driven by hydrofracturing and ice cliff failure. *Earth and Planetary Science Letters*, *412*, 112–121. Retrieved from http://dx.doi.org/10.1016/j.epsl.2014.12.035 doi: 10.1016/j.epsl.2014.12.035

Pollard, D., Gomez, N., DeConto, R., & Han, H. K. (2018). Estimating Modern Elevations of Pliocene Shorelines Using a Coupled Ice Sheet-Earth-Sea Level Model. *Journal Geophysical Research: Earth Surface*, 1–13. doi: 10.1029/2018JF004745

Pollard, D., Gomez, N., & DeConto, R. M. (2017). Variations of the Antarctic Ice Sheet in a Coupled Ice Sheet-Earth-Sea Level Model: Sensitivity to Viscoelastic Earth Properties. *Journal of Geophysical Research: Earth Surface*, *122*(11), 2124–2138. doi: 10.1002/2017JF004371

Rasmussen, C. E., & Williams, C. K. I. (2006). *Gaussian processes for machine learning (adaptive computation and machine learning)*. The MIT Press.

Rasmussen, D. J., Bittermann, K., Buchanan, M. K., Kulp, S., & Strauss, B. H. (2018). Extreme sea level implications of 1.5 C, 2.0 C, and 2.5 C temperature stabilization targets in the 21st and 22nd centuries. *Environmental Research Letters*, *13*.

Rasmussen, D. J., Buchanan, M. K., Kopp, R. E., & Oppenheimer, M. (2020). A Flood Damage Allowance Framework for Coastal Protection With Deep Uncertainty in Sea Level Rise. *Earth's Future*, *8*(3), 1–16. doi: 10.1029/2019EF001340

Riahi, K., Rao, S., Krey, V., Cho, C., Chirkov, V., Fischer, G., ... Rafaj, P. (2011). RCP 8.5-A scenario of comparatively high greenhouse gas emissions. *Climatic Change*, *109*(1), 33–57. doi: 10.1007/s10584-011-0149-y

Rignot, E., Mouginot, J., van den Broeke, M., van Wessem, M. J., Morlighem, M., & Scheuchl, B. (2019). Four decades of Antarctic Ice Sheet mass balance from 1979–2017. *Proceedings of the National Academy of Sciences*, *116*(4), 1095–1103. doi: 10.1073/pnas.1812883116

Robel, A. A., Seroussi, H., & Roe, G. H. (2019). Marine ice sheet instability amplifies and skews uncertainty in projections of future sea-level rise. *Proceedings of the National Academy of Sciences*, 201904822. Retrieved from `http://www.pnas.org/lookup/doi/10.1073/pnas.1904822116` doi: 10.1073/pnas.1904822116

Rohling, E. J., Grant, K., Hemleben, C., Siddall, M., Hoogakker, B. A. A., Bolshaw, M., & Kucera, M. (2008). High rates of sea-level rise during the last interglacial period. *Nature Geoscience*, *1*(1), 38–42. doi: 10.1038/ngeo.2007.28

Rohling, E. J., Hibbert, F. D., Grant, K. M., Galaasen, E. V., Irvalı, N., Kleiven, H. F., ... Yu, J. (2019). Asynchronous Antarctic and Greenland ice-volume contributions to the last interglacial sea-level highstand. *Nature communications*, *10*(1), 5040. doi: 10.1038/s41467-019-12874-3

Rohling, E. J., Hibbert, F. D., Williams, F. H., Grant, K. M., Marino, G., Foster, G. L., ... Yokoyama, Y. (2017). Differences between the last two glacial maxima and implications for ice-sheet, δ18O, and sea-level reconstructions. *Quaternary Science Reviews*, *176*, 1–28. Retrieved from `https://doi.org/10.1016/j.quascirev.2017.09.009` doi: 10.1016/j.quascirev.2017.09.009

Santner, T. J., Williams, B. J., & Notz, W. I. (2003). *The design and analysis of computer experiments*. Springer New York. Retrieved from `https://doi.org/10.1007\%2F978-1-4757-3799-8` doi: 10.1007/978-1-4757-3799-8

Scherer, R. P., Aldahan, A., Tulaczyk, S., Possnert, G., Engelhardt, H., & Kamb, B. (1998). Pleistocen collapse of the West Antarctic ice sheet. *Science*, *281*(5373), 82–85. doi: 10.1126/science.281.5373.82

Schoof, C. (2007). Ice sheet grounding line dynamics: Steady states, stability, and hysteresis. *Journal of Geophysical Research: Earth Surface*, *112*(3), 1–19. doi: 10.1029/2006JF000664

Seroussi, H., Nowicki, S., Payne, A., Goelzer, H., Lipscomb, W., Abe Ouchi, A., ... Zwinger, T. (2020). ISMIP6 Antarctica: a multi-model ensemble of the Antarctic ice sheet evolution over the 21st century. *The Cryosphere Discussions*(January), 1–54. doi: 10.5194/tc-2019-324

Silverman, B. W. (1986). *Density estimation for statistics and data analysis*. London: Chapman & Hall.

Stammer, D., van de Wal, R., Nicholls, R., Church, J., Le Cozannet, G., Lowe, J., ... Hinkel, J. (2019). Framework for high-end estimates of sea-level rise for

stakeholder applications. *Earth's Future*, 1–16. doi: 10.1029/2019ef001163

Steig, E. J., & Neff, P. D. (2018). The prescience of paleoclimatology and the future of the Antarctic ice sheet. *Nature Communications*, *9*(1), 11–13. Retrieved from `http://dx.doi.org/10.1038/s41467-018-05001-1` doi: 10.1038/s41467-018-05001-1

Weertman, J. (1974). Stability of the Junction of an Ice Sheet and an Ice Shelf. *Journal of Glaciology*, *13*(67), 3–11. doi: 10.3189/s0022143000023327

Wise, M. G., Dowdeswell, J. A., Jakobsson, M., & Larter, R. D. (2017). Evidence of marine ice-cliff instability in Pine Island Bay from iceberg-keel plough marks. *Nature*, *550*(7677), 506–510. Retrieved from `http://dx.doi.org/10.1038/nature24458` doi: 10.1038/nature24458

Wong, T. E., Bakker, A. M., & Keller, K. (2017). Impacts of Antarctic fast dynamics on sea-level projections and coastal flood defense. *Climatic Change*, *144*(2), 347–364. doi: 10.1007/s10584-017-2039-4

Supporting Information for "Could the Last Interglacial Constrain Projections of Future Antarctic Ice Mass Loss and Sea-level Rise?"

Daniel M. Gilford[1,2], Erica L. Ashe[2], Robert M. DeConto[3], Robert E. Kopp[1,2], David Pollard[4], Alessio Rovere[5]

[1]Institute of Earth, Ocean, and Atmospheric Sciences, Rutgers University, 71 Dudley Road, Suite 205, New Brunswick, NJ 08901, USA.

[2]Department of Earth and Planetary Sciences, Rutgers University, Piscataway, NJ, USA.

[3]Department of Geosciences, University of Massachusetts, Amherst, MA, USA.

[4]Earth and Environmental Systems Institute, Pennsylvania State University, University Park, PA, USA.

[5]MARUM, Center for Marine Environmental Sciences, University of Bremen, Germany.

Contents of this file

1. Introduction

2. Tables S1 and S2

3. Text S1

4. Text S2

5. Figures S1 to S10

6. Glossary: Table S3

Introduction

This supporting information provides underlying details on the ice-sheet model ensemble, emulator construction, validation, and sensitivity tests, as well as supplemental figures of timeseries color-coded by CREVLIQ, comparisons between the Last Interglacial and RCP8.5 ensembles across the model parameter space, conditional posterior distributions in 2150, and ice-sheet model parameter likelihoods as a function of LIG constraint distribution. We note that the ice-sheet model ensembles are constructed with a model version updated since DeConto and Pollard (2016), but predating that of DeConto et al. (2020). As such, the results herein are not representative of the most current results with the latest physical model, but are illustrative of how ice-sheet models may be combined with statistical/machine learning methods and paleoclimate evidence to (a) constrain projections of future Antarctic ice-sheet contributions to sea-level rise, and to (b) identify how improved paleo sea level estimates could inform projections. A glossary of key study terms is included at the end, for reference.

Table S1. Ice-sheet model parameter values used to construct a 14×14 grid composing 196 members for the Last Interglacial and RCP8.5 scenario ensembles.

CLIFVMAX ($\frac{\text{km}}{\text{yr}}$)	CREVLIQ ($\frac{\text{m}}{(\text{myr}^{-1})^2}$)
0	0
1	15
2	30
3	45
4	60
5	75
6	90
7	105
8	120
9	135
10	150
11	165
12	180
13	195

Table S2. Optimized hyperparameters of the GP models (Eqn. 1–3) found by maximizing the log-likelihoods, given the training ensembles.

Ensemble	α_1^2 (m^2)	ℓ_1^2	α_2^2 (m^2)	ℓ_2^2	τ (yr)
LIG	17.048	45.698	—	—	—
RCP8.5	2731.8	2.7567	1.830	0.50121	95.52198

Text S1. Emulator Leave-one-out Analyses

To assess whether the Gaussian process (GP) model emulator accurately mimics the ice-sheet simulator, we perform a leave-one-out (LOO) analysis following a modification of the methodology of Bastos and O'Hagan (2009). We calculate the individual standardized prediction errors as,

$$D_j^I = \frac{z_j - E[f(\theta_\mathbf{1}, \theta_\mathbf{2})_j | \mathbf{z}_{\backslash \mathbf{j}}]}{\sqrt{V[f(\theta_\mathbf{1}, \theta_\mathbf{2})_j | \mathbf{z}_{\backslash \mathbf{j}}]}} \tag{S1}$$

where $\mathbf{z_{\backslash j}}$ is the vector composed all of training ensemble members in $\mathbf{z}$ except z_j at the jth location in model parameter space (i.e. the value with a fixed [θ_1,θ_2] from Table S1, removed for the LOO process), and $E[\cdot]$ and $V[\cdot]$ are the expectation (mean function) and variance, respectively, of the optimized emulator conditioned on $\mathbf{z_{\backslash j}}$. For RCP8.5, f and $\mathbf{z_{RCP}}$ are a function of time, and hence D_j^I is also time-dependent. The LIG emulator, $\mathbf{z_{LIG}}$, and the LIG standardized prediction errors have no time dependency. Errors are shown for the LIG in Figure S3 and the RCP8.5 scenario (in 2000, 2050, 2100, and 2150) in Figure S4.

Standardized errors are expected to follow a standard Student-t distribution. Errors which consistently exceed ±2 (the 95% credibility interval) indicate a conflict between the emulator and simulator (Bastos and O'Hagan 2009). We find that the LIG and RCP8.5 emulators performs well, with nearly all errors falling within the confidence interval. Emulator skill degrades slightly over the time in the RCP8.5 scenario as the training data sea-levels disperse when instabilities drive mass loss (section 3.2), creating less densely packed training information in time and parameter space. 5/196, about 2.5%, of the errors exceed +2 in 2150. These poorly performing emulator estimates are located near the exterior of parameter space, where θ_1 and θ_2 are high, and there is less surrounding training information to constrain the emulator prediction (behavior which is typical of trained Gaussian process models, Rasmussen and Williams 2006).

Across time and both training ensembles, standardized emulator errors are less than ±2 in over 99% of points tested. One concern might be whether these errors indicate emulator variances are too large relative to the mean (i.e. whether the model is underconfident), driving low values of D_j^I. The RCP8.5 emulator very accurately predicts relatively small (near-zero) and broadly similar changes in mass loss across the whole parameter space; this contributes to the model's excellent standardized agreement through 2050 (Fig. S4, top panels). As the distribution of

ice-sheet mass begins to diverge around 2060 (Fig. 3) and emulator skill drops marginally (as discussed above), the model evolves toward an error distribution more consistent with the expected standard Student-t distribution. Overall, the time-independent variance of the RCP8.5 emulator is always <0.0004 m^2 across the model parameter space, such that the model standard deviation is always <2 cm.

The LIG emulator variance is plotted in Figure S7; values span over 0–0.016 m^2 across the ice-sheet model parameter space. The associated GP model standard deviation is 11 cm on average, $\sim$3% of the range of the LIG emulator output. The model may therefore be slightly underconfident, which could affect our study results/conclusions in two ways. First, a model with too high variance would result in less confidence in model parameters given a specific LIG constraint (i.e. less polarized likelihoods, Fig. S5), so that the LIG is less informative for the MICI process. Second, higher variance results in a broader emulated distribution than may be warranted. However, one of the strengths of the Bayesian approach (section 2.3) is the ability both include and quantify the uncertainty of the emulator (as in Fig. S7), so some variance in the final model is justified. Ultimately, the final model described in the main text captures the key behavior of the training data, and had the smallest variances of any model explored (cf. Text S2).

Overall, performance is consistent with that of another recently published ice-sheet model emulator (Edwards et al. 2019, their Extended Data Figure 6), which was trained on a different version of the same ice-sheet model (e.g., Pollard and DeConto 2012). We conclude the emulator is able to accurately predict simulator responses across the LIG and RCP8.5 scenarios with appropriate uncertainties.

Text S2. GP Model Selection and Sensitivity to Covariance Function

There are infinitely many possible model forms, specifications, optimization targets, etc. to consider for an emulator (Rasmussen and Williams 2006). The "final model" (described in the main text) represents the best model based on several metrics: model simplicity, likelihood maximization, and minimizing of prediction errors (described above in Text S2) and model uncertainty (i.e. posterior variance).

We assessed different covariance forms: squared-exponential functions (sometimes called the radial basis function), nonstationary linear (sometimes called dot-product) functions, and Matérn functions with shape parameters (ν) of $\frac{1}{2}$, $\frac{3}{2}$, and $\frac{5}{2}$. We also evaluated various combinations of these functions, and experimented with specifying them along the individual axes of the training data (θ_1, θ_2, and time). For instance, we considered the complex form,

$K(\theta_1, \theta_2) \sim Linear(\theta_1) * Matérn_{\nu=\frac{5}{2}}(\theta_1) + Linear(\theta_2) * Matérn_{\nu=\frac{5}{2}}(\theta_2) + Matérn_{\nu=\frac{5}{2}}(\theta_1, \theta_2)$.

Trained models produced log-likelihoods similar to (or sometimes even higher than) the final model. But when optimized, each of these models required a variance (fit uncertainty) larger than the final model (Fig. S7) in order to match the training data (cf. Text S2). Under such circumstances, the optimized model is underconfident, and a nugget of 10^{-6} m is a strong requirement that is inconsistent with the optimized model variance. We present one such model as an example below and discuss the implications.

To demonstrate the emulator sensitivity to the choice of covariance function, we specify an alternative set of covariance functions, f_1^* and f_2^*, which replace f_1 and f_2 in Eqn. (1):

$$f_1^*(\theta_1, \theta_2) \sim \mathcal{GP}(0, \alpha_1^2 K_{1,\theta_1}(\theta_1, \theta_1'; \ell_{1,\theta_1}) \cdot K_{1,\theta_2}(\theta_2, \theta_2'; \ell_{1,\theta_2})), \tag{S2}$$

$$f_2^*(\theta_1, \theta_2, t) \sim \mathcal{GP}(0, \alpha_2^2 K_{2,\theta_1}(\theta_1, \theta_1'; \ell_{2,\theta_1}) \cdot K_{2,\theta_2}(\theta_2, \theta_2'; \ell_{2,\theta_2}) \cdot K_t(t, t'; \tau)), \tag{S3}$$

where there are four distinct covariance functions, $K_{i,\theta}$, each with a unique and trainable length scale specified along either CLIFVMAX (θ_1) or CREVLIQ (θ_2), $\ell_{i,\theta}$. Because the model form is different, the hyperparameters which share an interpretation with Eqn. (1)—α_i and τ—need not have the same optimized values as those of the final model (Table S2). Following the procedure described in sections 2.2–2.3, this alternative model is optimized and conditioned on the training simulations, and its posterior distributions are found conditional on LIG constraints.

The unconstrained Last Interglacial distribution of this alternative model form is presented in Figure S8 alongside the final model distribution (reproduced from Fig. 4a) and the LIG training ensemble histogram. The alternative model distribution is broader than that of the final model distribution, driven by a larger variance. The LIG alternative model's average standard deviation is 25 cm, more than twice that of the final model, which smooths out some of the multi-modal features of the unconstrained LIG distribution. The training ensemble exhibits a multi-modal distribution (more consistent with the final model), suggesting the alternative model contributes less information about AIS mass loss from individual sectors than indicated by the original ice-sheet model simulations.

Likewise, the alternative model of the RCP8.5 emulator has greater uncertainty, with a time-constant standard deviation of $\sim$5 cm and a width of the 95% credibility interval between 2000 and 2060 of 20 cm (a period where the full range of simulated mass loss is 0–7.7 cm). Given these increased uncertainties, emulated behavior such as the instability-driven skew in Fig. 7b (given a relatively low LIG constraint) disappears, suggesting the alternative model is less physical. The alternative model posterior distributions of RCP8.5 AIS mass loss as a function of LIG constraints are shown in Figure S9. Comparing with Fig. 4b, posterior distributions have substantially broader projections if the LIG was known precisely (to within 10 cm). This degrades

the informative power of LIG constraints on the margins of the LIG distribution (i.e. high or low values, Fig. 7b), because the baseline uncertainty more than doubles. Hence, the final model more accurately captures the multi-modal behavior of the LIG training ensemble and is more precise in its predictions.

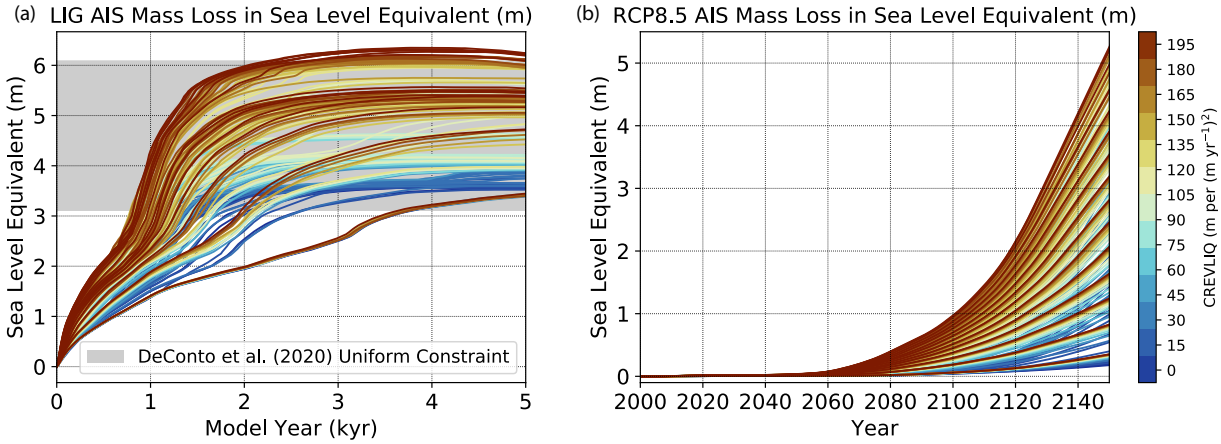


Figure S1. As in Fig. 1, except timeseries are color-coded by their CREVLIQ values over 0–195 $\frac{\text{m}}{(\text{myr}^{-1})^2}$.

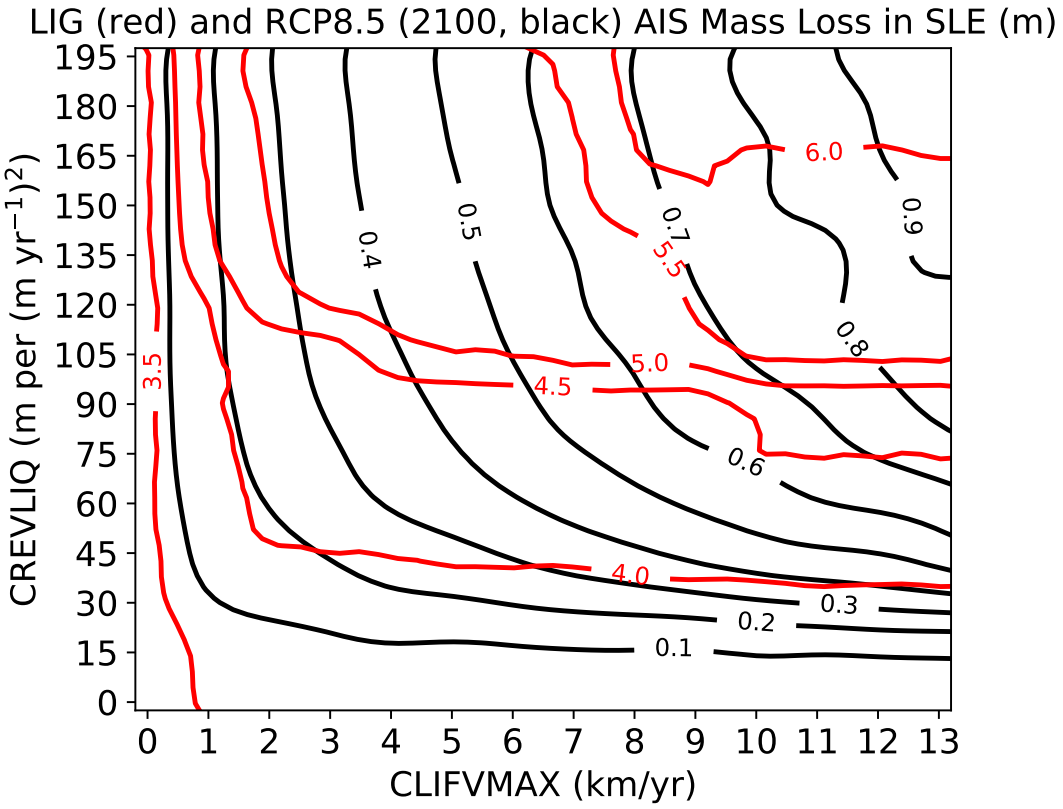


Figure S2. Contours are identical to the mean emulated sea-level contributions from the Antarctic ice sheet in Fig. 2, but with LIG and RCP8.5 contours overlapping for comparison.

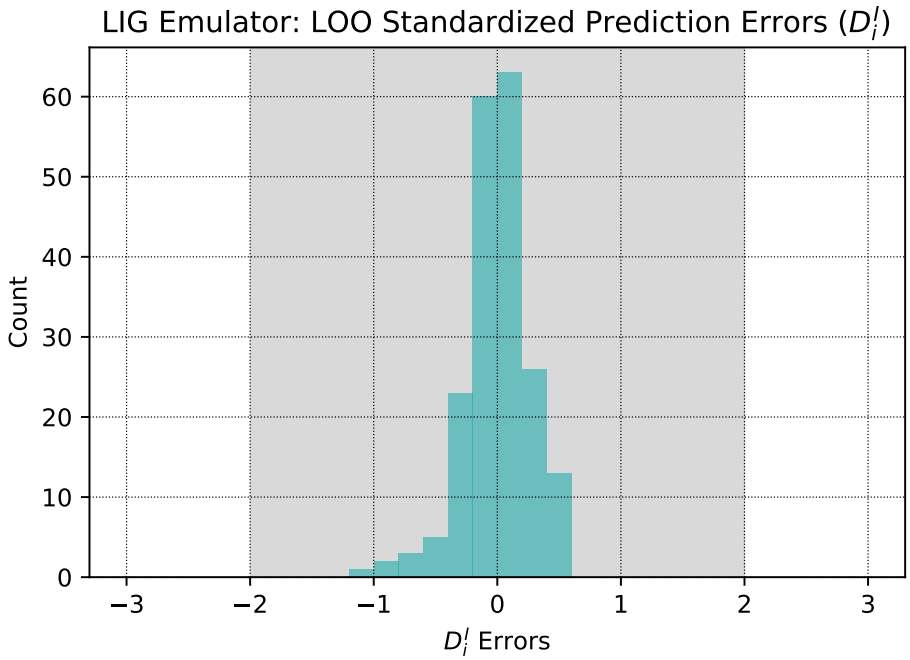


Figure S3. Histogram of standardized prediction errors (Eqn. S1) from leave-one out analyses performed with the Last Interglacial emulator. Errors $< \pm 2$ (gray shaded region) indicate the emulator is able to properly represent the ice-sheet model (cf. Bastos and O'Hagan, 2009).

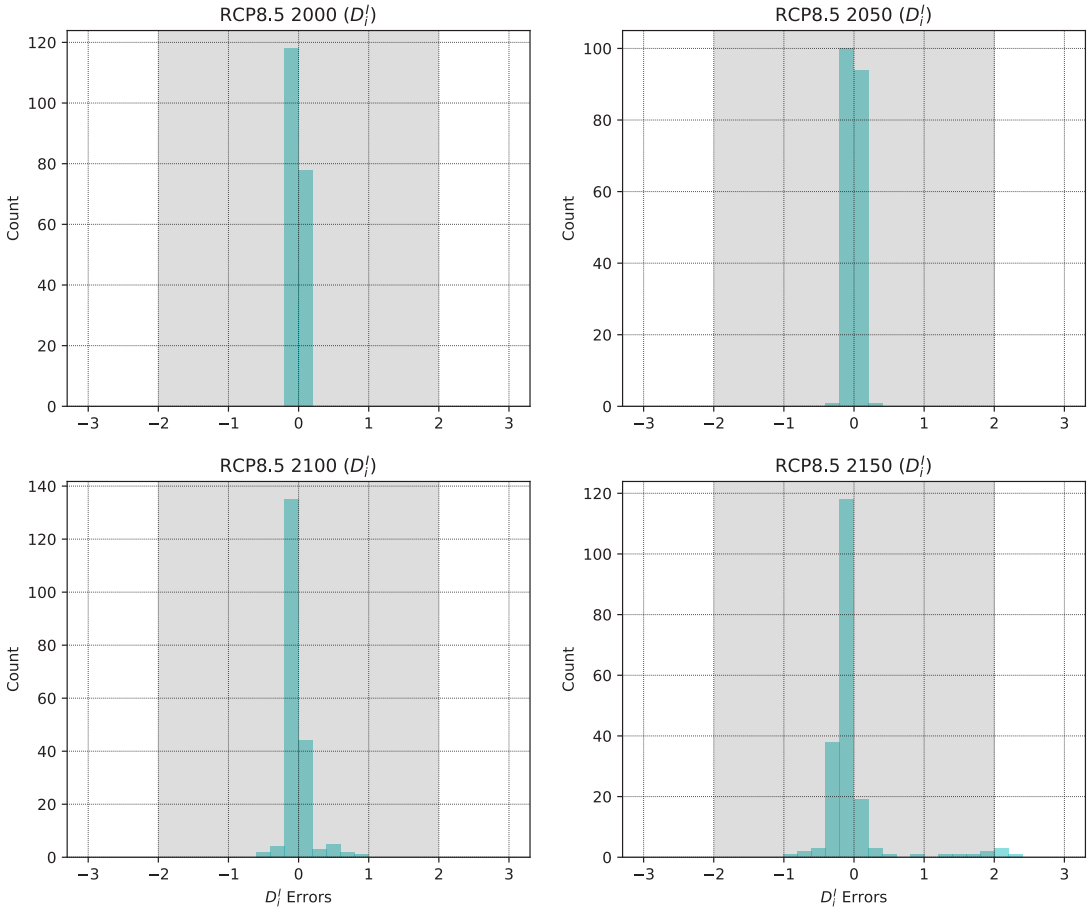


Figure S4. As in Fig. S3, but for the RCP8.5 emulator in 2000, 2050, 2100, and 2150.

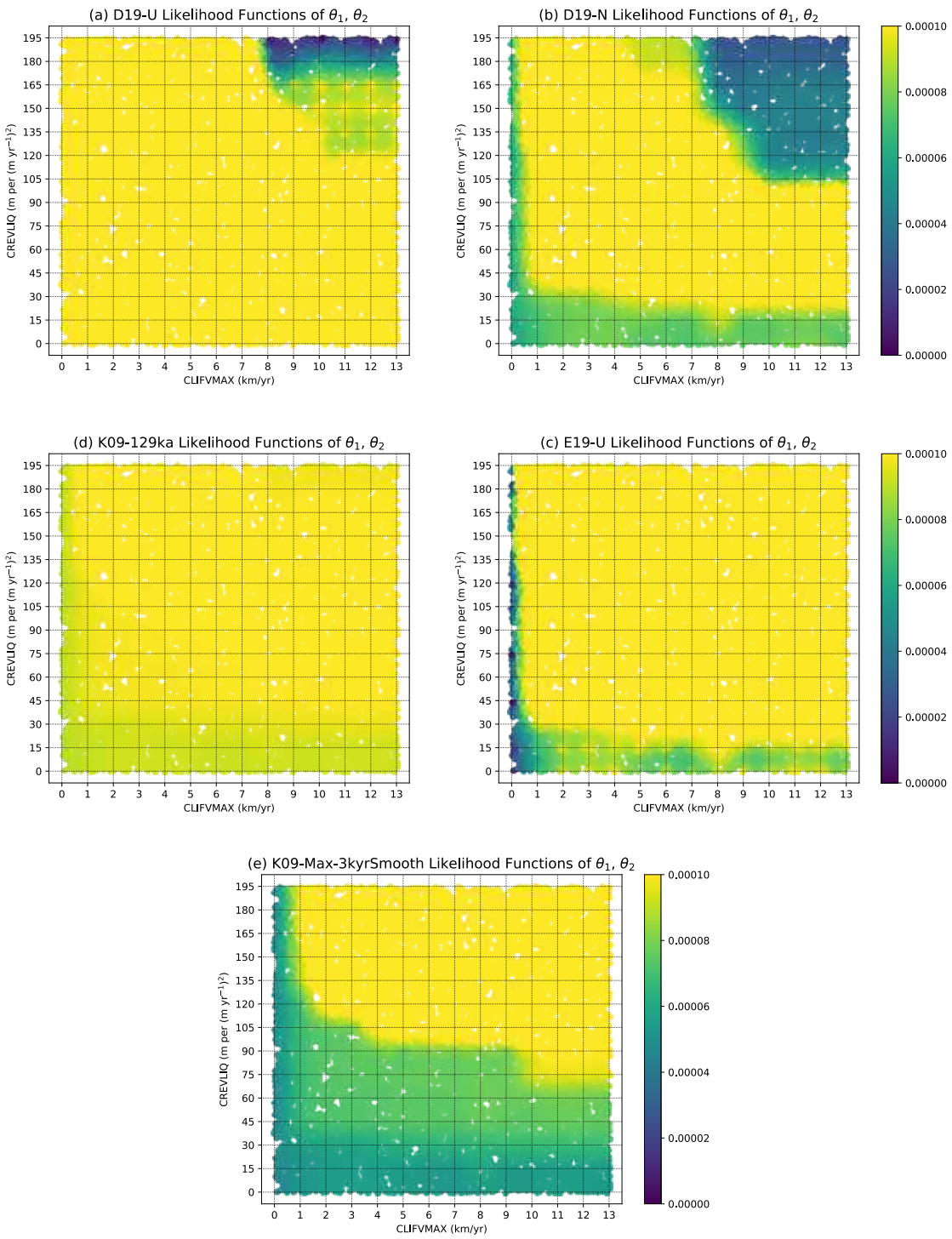


Figure S5. The posterior probabilities of CREVLIQ/CLIFVMAX latin-hypercube sampled pairs across the range of the model ensemble parameter space (cf. Table S1), conditional on specified constraints on Last Interglacial Antarctic Ice-sheet sea level contributions (cf. Figure 4a). The colorbar saturates at it upper extent.

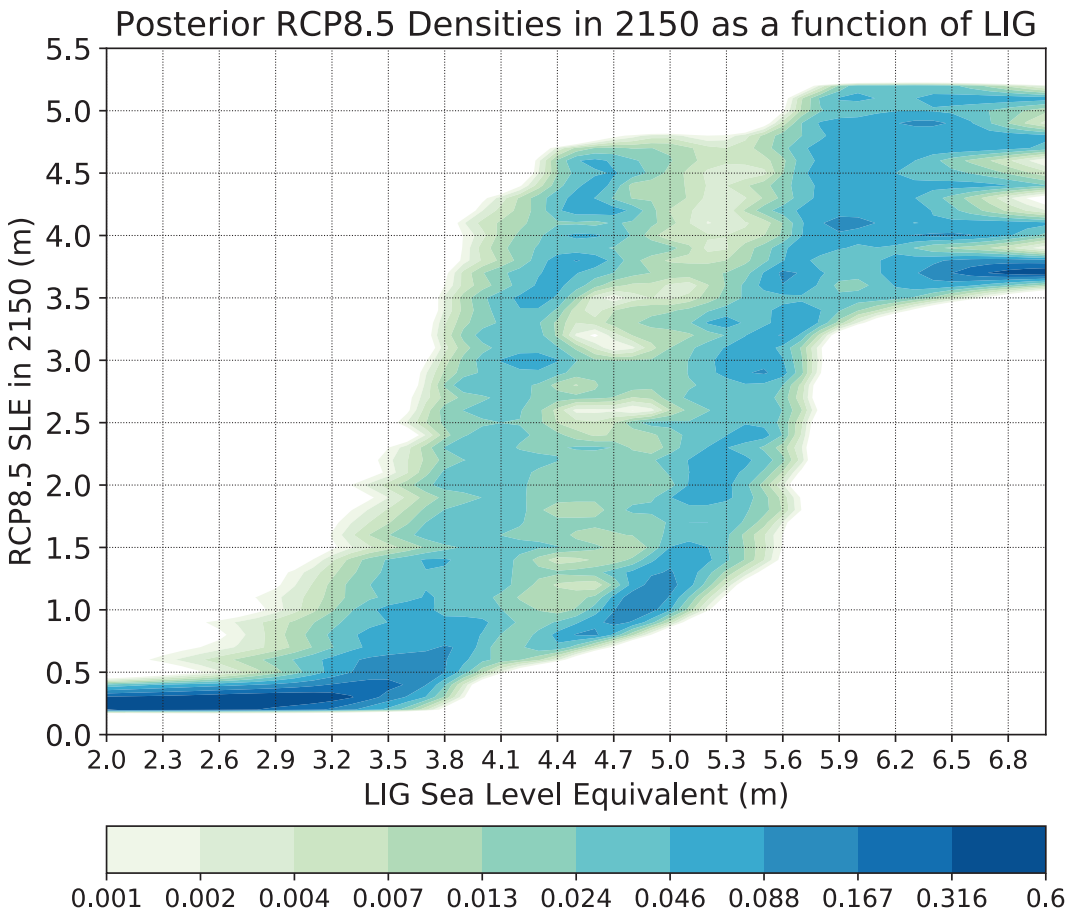


Figure S6. As in Fig. 4b, except for 2150.

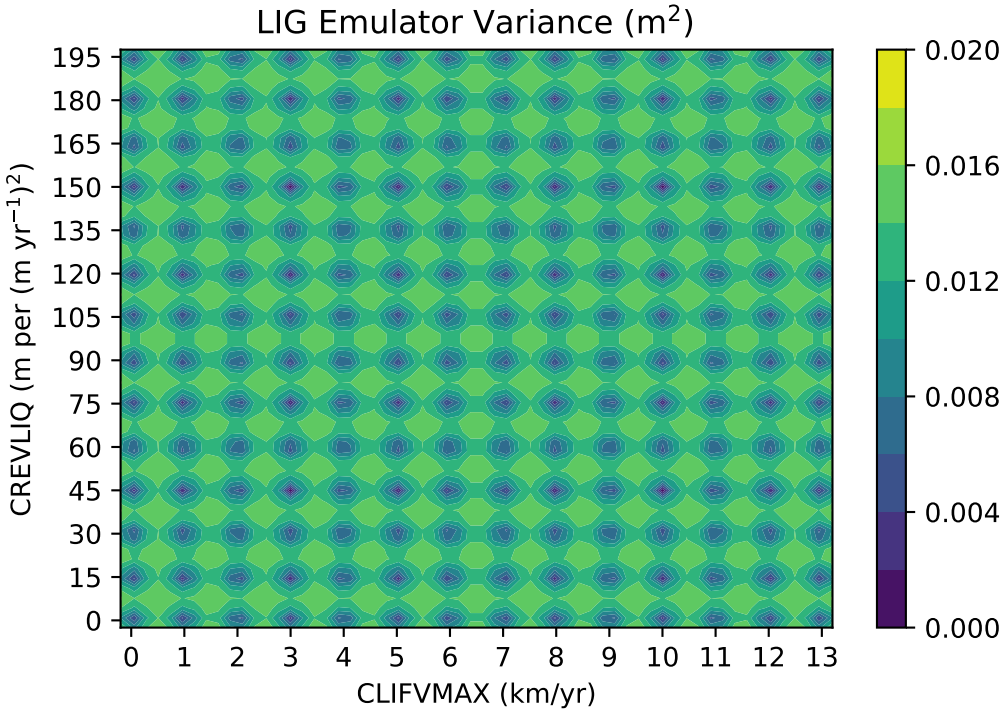


Figure S7. Last Interglacial emulator variance (m^2) over the ice-sheet model parameter space.

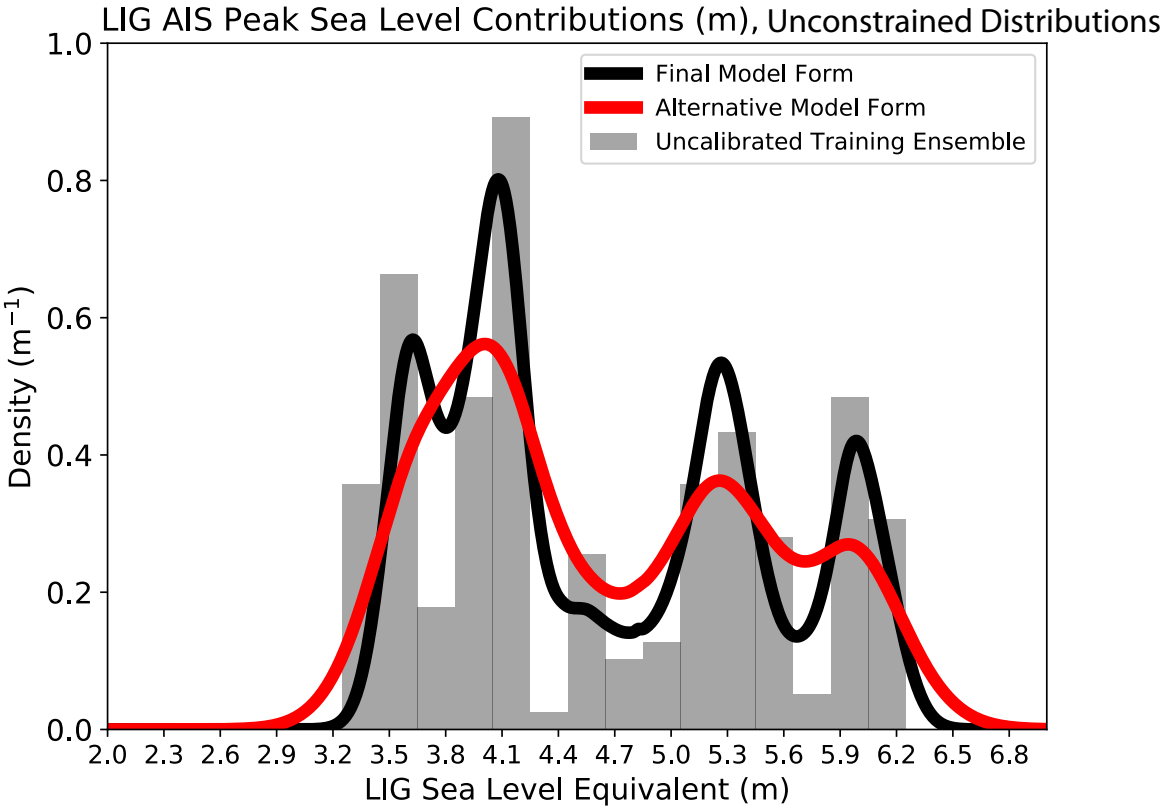


Figure S8. Unconstrained Last Interglacial emulated distribution reproduced from Fig. 4a (black curve), compared with the emulated distribution from an alternative model (red curve) defined with the covariance functions given in Eqn. (S2–S3). The training ensemble is shown as a histogram scaled for comparison.

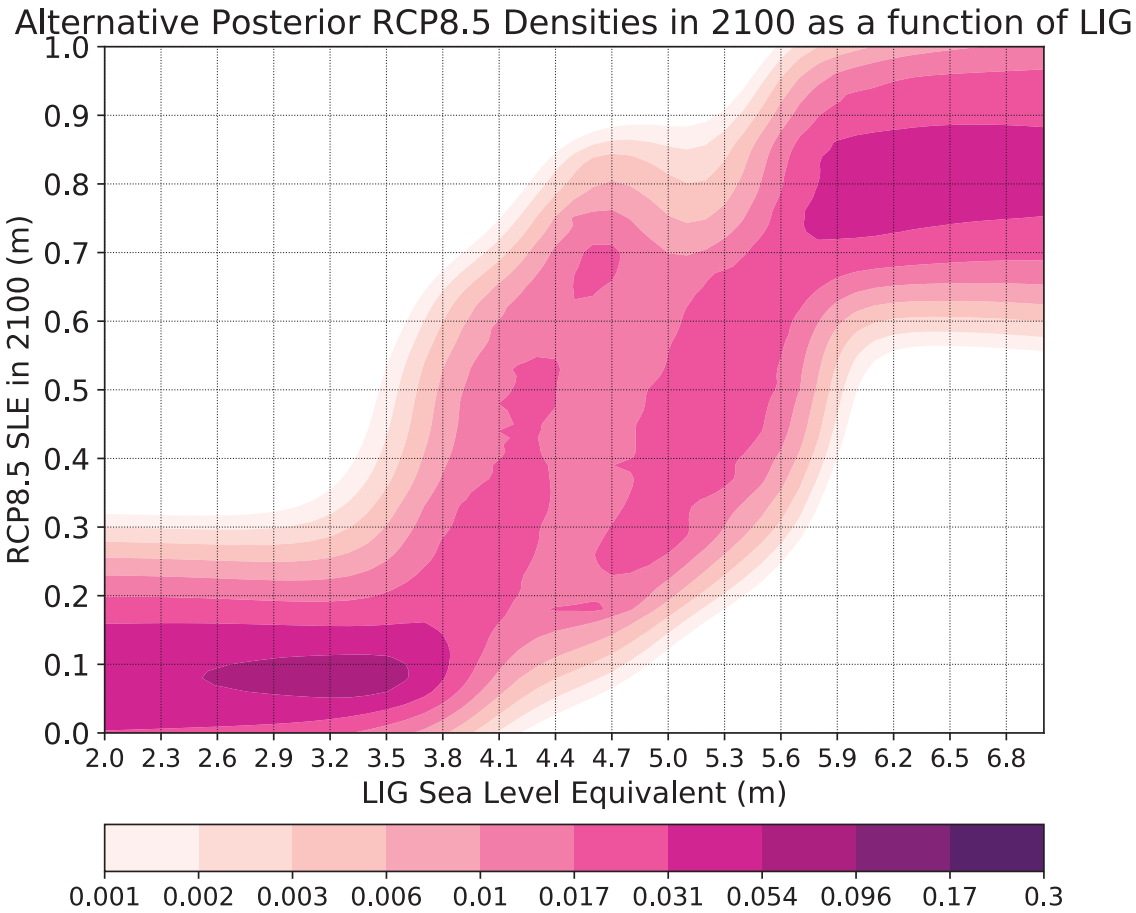


Figure S9. As in Fig. 4b, except normalized conditional posterior probability densities are plotted as a function of Last Interglacial AIS mass loss emulated with an alternative model defined with the covariance functions given in Eqn. (S2–S3).

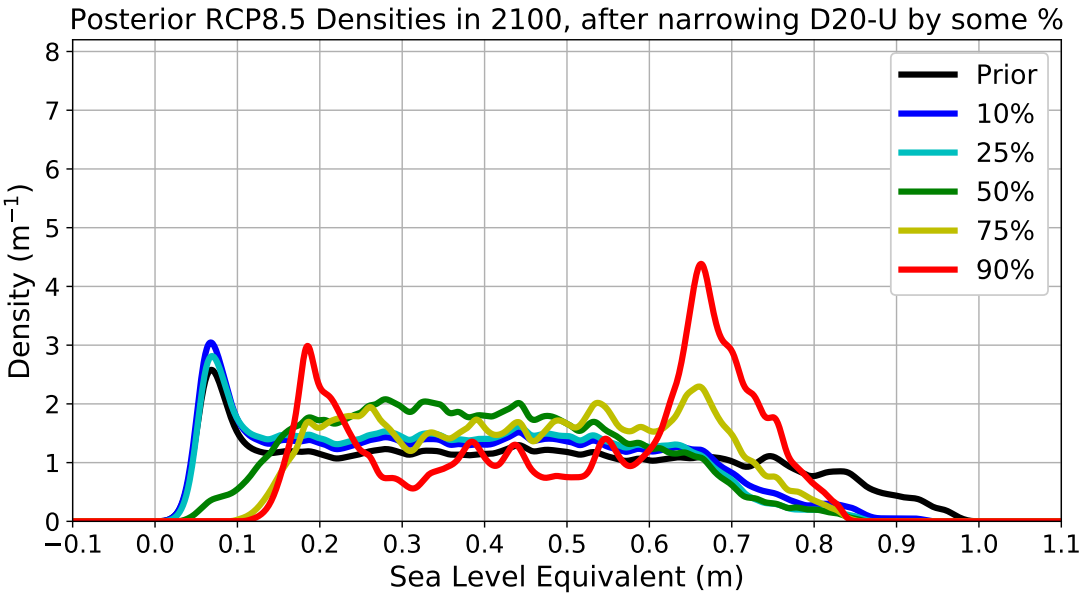


Figure S10. As in Fig. 6, except posteriors are constrained assuming the D20-U constraint was 10%, 25%, 50%, 75% or 90% narrower (blue, cyan, green, yellow and red curves, respectively).

Table S3. Glossary—Definitions of relevant terms.

Term	Meaning
Bayesian statistics	(in contrast to frequentist or classical statistical inference) is a theory based on the Bayesian interpretation of probability where probability expresses a degree of belief in an event. Bayesian methods compute a posterior probability of a model or parameter through the use of a prior probability distribution of the model or parameter times a likelihood function using Bayes' theorem
Bayesian updating	the process of using new information to improve on previous estimates. One uses the posterior distribution of one model as the likelihood of a new model. For example, the posterior distribution on the ice-sheet model parameters, $(\theta_1, \theta_2 \mid f_{LIG})$, is used as the likelihood distribution in the future projection model
Conditional probability	the distribution of a random quantity, given (assuming, or as a function of) a particular value of another random quantity
Covariance function	defines prior beliefs about the relationship between one or more variables or parameters in a Gaussian process, as a measure of how much they change together
Gaussian process (GP)	a generalization of the multi-variate Gaussian distribution to continuous parameter space, which is fully defined by its mean function and covariance function; GP regression provides an analytically-tractable solution when adopting the assumption of normality for all distributions
Hyperparameter	parameter of a GP model prior distribution
Likelihood	the probability of observing the data as described by the fitted model; also known as the sampling or data distribution; a conditional distribution that is a function of unknown parameters for observed data
Marginal distribution	unconditional probability distribution of a random quantity, found by integrating over all values of the conditional distribution

Table S3 ***(continued).***

Term	Meaning
Non-parametric	not involving any assumptions as to the functional form
Posterior probability	the probability distribution of an unknown quantity, conditional on (or assuming/given) observed data; In this study these are, 1) the future AIS sea-level contribution projections over time conditioned on a specified Last Interglacial estimate distribution, and 2) the distribution of the model parameters (CREVLIQ and CLIFVMAX) given specific LIG constraints
Prior probability	(of an uncertain quantity—e.g., parameter or model) uses a priori beliefs about the quantity before some evidence or data is taken into account; the prior is combined with the probability distribution of new data to yield a posterior distribution. The prior can be subjective or uninformative (such as a uniform distribution) to minimize the impact on Bayesian statistics